The Pennsylvania State University
The Graduate School
College of Engineering

PERFORMANCE EVALUATION AND OPTIMIZATION OF AN 8-GHz MICROWAVE ELECTROTHERMAL THRUSTER

A Thesis in
Aerospace Engineering
by
Jacob H. Blum

Submitted in Partial Fulfillment
of the Requirements
for the Degree of

Master of Science

May 2009

The thesis of Jacob H. Blum was reviewed and approved* by the following:

Michael M. Micci
Professor of Aerospace Engineering and Director of Graduate Studies
Thesis Advisor

Sven G. Bilén
Associate Professor of Engineering Design, Electrical Engineering, and Aerospace Engineering

George A. Lesieutre
Professor of Aerospace Engineering and Department Head of Aerospace Engineering

*Signatures are on file in the Graduate School

ABSTRACT

The performance of an 8-GHz microwave electrothermal thruster was measured using various thrust stand configurations with nitrogen gas as the propellant. The momentum of the exhausted propellant was transferred to the flexible beam by either a momentum trap or a deflection cone. The thrust stand used either a strain gauge or an optical distance sensor to measure the deflection of the flexible beam, which was ultimately converted into thrust measurements. The thruster was also optimized by parametrically testing a variety of different thruster components, including antenna depth, propellant injector cross-sectional diameter, nozzle material and throat diameter, and propellant gas type. Input powers ranging from 100 W to 350 W were used to induce electrical breakdown of the propellant gas (nitrogen, ammonia, and simulated decomposed hydrazine) and form a coalesced plasma.

The thrust stand configuration that used a strain gauge and momentum trap produced thrust values within 3% of the theoretically calculated thrust. However, this configuration could not measure low thrust values. The thrust stand configuration that used a strain gauge and deflection cone was able to measure low thrust values; however, the thrust measurement procedure illustrated measurement contradictions, producing thrust values within both 0.7% and 11% of theoretical thrust values. The thrust stand configuration using the deflection cone and optical distance sensor eliminated the measurement contradictions; however, the configuration continued to provide thrust measurements that differed from the theoretical thrust calculations by upwards of 12%.

The thruster configuration that achieved the highest specific impulse, thermal efficiency, and thruster efficiency is considered the optimal configuration. This experimentally determined optimal configuration used ammonia propellant and consisted of a two piece chamber separated by a separation plate; an antenna with a flat tip and a protruding depth 75% reduced from the baseline configuration; the smallest possible propellant injector diameter that does not choke the flow; and a stainless steel nozzle with a throat diameter 235% greater than the baseline nozzle throat diameter. This produced thermal and thruster efficiencies of approximately 75% and a specific impulse 33% higher than the highest specific impulse ever achieved by any microwave electrothermal thruster experiment using ammonia as the propellant. Recommendations for achieving more accurate thrust measurements as well as further thruster optimization are also discussed.

TABLE OF CONTENTS

LIST OF FIGURES

NOMENCLATURE

A	Area, m^2
A^*	Throat area, m^2
A_e	Exit area, m^2
A_{mn}	Amplitude constant
A_z	Magnetic vector potential, HA/m
B_{mn}	Vector potential constant, HA/m
C	Capacitance, F
CS	Control surface, m^2
CV	Control volume, m^3
C_d	Discharge coefficient
c_p	Specific heat at constant pressure, J/kg K
c_v	Specific heat at constant volume, J/kg K
c^*	Characteristic velocity, m/s
C_τ	Thrust coefficient
d^*	Throat diameter, m
E	Electric field, V/m
E_t	Threshold electric field strength, V/m
e	Internal energy, J/kg
F	Force, N
f_{res}	Resonant frequency, Hz
G	Shunt conductance, S
g	Gravitational acceleration, m/s^2; Gibbs free energy, J
g^0	Standard state free energy, J
H	Magnetic field, A/m
h	Enthalpy, J/kg
h_0	Total enthalpy, J/kg
h_c	Chamber enthalpy, J/kg
h_e	Exit enthalpy, J/kg
I	Current, A
I^*	Complex conjugate of current, A
I_{sp}	Specific Impulse, s
i	Time dependant current, A
J	Number of chemical species
J_m	Bessel function
J'_m	First derivative of Bessel function
j	imaginary constant, $\sqrt{-1}$
K_p	Equilibrium constant
L	Inductance, H
M	Mach number
$\dot{m}$	Mass flow rate, kg/s
$\dot{m}^*$	Throat mass flow rate, kg/s
P	Power, W
P_{abs}	Absorbed power, W
P_{av}	Average power, W
P_d	Dissipated power, W
P_{for}	Forward power, W
P_{input}	Input power, W
P_{ref}	Reflected power, W
P_τ	Thrust power, W
p	Pressure, Pa
p_0	Total pressure, Pa
p_a	Ambient pressure, Pa
p_c	Chamber pressure, Pa

p_e	Exit pressure, Pa
p^0	Reference pressure, Pa
Q	Quality factor
q	Heat, J/kg
$\dot{q}$	Heat flux, J/kg s
R	Specific gas constant, J/kg K;
	Resistance, Ω
R_e	Reynold's number
R_s	Surface resistance, Ω
s	Entropy, J/kg K
T	Temperature, K
T_0	Total temperature, K
T_c	Chamber temperature, K
T_e	Exit temperature, K
u	Velocity, m/s
u_c	Chamber velocity, m/s
u_e	Exit velocity, m/s
u_{eq}	Equivalent exhaust velocity, m/s
u^*	Throat velocity, m/s
V	Volume m^3; Voltage V
v	Specific volume, m^3/kg;
	Time dependant voltage, V
W	Total stored energy, J
w	Work, J/kg
X	Reactance, Ω
X_j	Mole fraction
Z	Impedance, Ω
β	Phase constant
Γ	Voltage reflection coefficient
γ	Ratio of specific heats;
	Complex propagation constant
Δ	Change in
ε	Permittivity, F/m;
	Progress of reaction
η_τ	Thruster efficiency
η_T	Thermal efficiency
Λ	Characteristic diffusion length, m
μ	Permeability, H/m
μ^*	Throat viscosity, kg/m s
ρ	Density, kg/m^3
ρ_0	Total density, kg/m^3
ρ^*	Throat density, kg/m^3
σ	Conductivity, S/m
τ	Thrust, N
χ_{mn}	Zeroes of Bessel function
ω	Angular frequency, Hz
∇	Del operator

ACKNOWLEDGMENTS

I would like to take this opportunity to thank a number of people who provided me with assistance, confidence, and guidance throughout my graduate school experience. I would like to thank Dr. Michael Micci, first, for giving me the opportunity to come to Penn State and perform research in his lab; and second, for his continual guidance and advice, and instilling in me the confidence needed to complete my degree. I have learned a great deal since becoming his graduate student. I would like to thank Dr. Sven Bilén for all of his assistance and direction. Many problems would not be solved had it not been for Dr. Bilén's suggestions and recommendations. I would like to thank Silvio Chianese for providing assistance and direction, as well as being understanding of my abilities and commitments; and Northrop Grumman Aerospace Systems for providing both the resources and motivation for the research project. I would to thank Mr. Bob Dillon for his expert machining skills and overall commitment to the project. I would like to thank my labmates, both past and current. Especially Dan Clemens for recommending and introducing me to the project; and Peter Hammond for his overall assistance with any problem I encountered in the lab, and for his advice on anything I happened to ask him. I would like to thank all faculty and staff in the Aerospace Department for all of their assistance through my time in graduate school. I would also like to thank my parents for their undying support, encouragement, and guidance not only through graduate school, but for my entire life. Finally I would like to thank the rest of my family and friends for providing support and encouragement through all my life's endeavors.

CHAPTER 1
Introduction

The Microwave Electrothermal Thruster (MET) is an experimental propulsion system that has been under development at The Pennsylvania State University since the mid 1980s. It is categorized as an electrothermal thruster that uses microwave energy to heat propellant gas. The goal of the MET research is to prove its capabilities and ultimately construct a space-ready system able to accomplish various space mission objectives. There has been much research performed on assorted frequency variations of the MET, including 2.45 GHz, 7.5 GHz, and 14.5 GHz. However, this thesis reports on the experimental performance evaluation and optimization of an intermediate power (100–350 W) 8-GHz MET.

1.1 Space Propulsion

Space propulsion systems are the means by which spacecraft and their payloads travel through space. There are many different types of space propulsion systems, all of which are intended for providing different degrees of spacecraft motion. These include the high power booster rockets, attitude adjusting thrusters, and even imaginative interplanetary propulsion devices. Of course the MET is included as a space propulsion device, but in order to specifically analyze and ultimately develop the MET, an analytical understanding of general rocket based propulsion must first be explored.

1.1.1 Analytical Foundations of Rocket Propulsion

Rocket propulsion is based on Newton's Third Law, which states that for every action, there is an equal and opposite reaction. The action is provided by the expulsion of mass from the rocket and the reaction is the force generated on the rocket, known as thrust. This phenomenon can be analytically represented by a control volume analysis using conservation of momentum,

$$\sum F_x = \frac{d}{dt}\int_{CV} \rho u_x dV + \int_{CS} u_x d\dot{m} \tag{1.1}$$

Figure 1.1 is a graphical representation of this generalized rocket control volume.

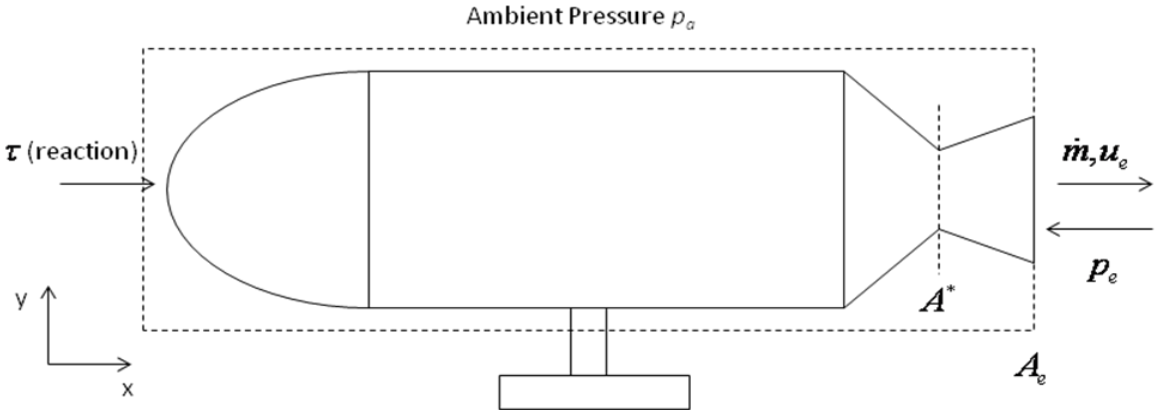

Figure 1.1 General rocket control volume

The force balance of the generalized rocket control volume is

$$\sum F_x = \tau + A_e p_a - A_e p_e \tag{1.2}$$

Using the assumption of steady flow and by combining and rearranging Equations (1.1) and (1.2), an equation for thrust, τ, is

$$\tau = \dot{m} u_e + (p_e - p_a) A_e \tag{1.3}$$

Thrust can be measured by determining the magnitude of the force needed to keep an operating rocket stationary and is expressed in units of pounds or newtons. For the sake of convenience, the thrust equation is often given in terms of equivalent velocity, u_{eq}, as[1]

$$\tau = \dot{m} u_{eq} \tag{1.4}$$

Thrust, as described above, is an important rocket performance parameter. However, the amount of propellant required for high thrust rockets is limited by factors such as cost and space. These limiting factors force propulsion systems to achieve greater efficiency in terms of amount of thrust per amount of propellant. The main efficiency parameter for rocket performance is called specific impulse, I_{sp}. Specific impulse is defined as the ratio of thrust to weight flow. It is expressed in units of seconds[1] as

$$I_{sp} = \frac{\tau}{\dot{m}g} = \frac{u_{eq}}{g} \tag{1.5}$$

1.1.2 Categorization of Propulsion Systems

Upon closer inspection of the thrust equation, performance increases can be achieved by either increasing mass flow or increasing exhaust velocity. While increasing mass flow is certainly important in designing high thrust rockets, this parameter is merely a reflection of the size of the rocket. However, the key to increasing performance of a rocket of a fixed size is to add energy to the system. This addition increases the kinetic energy of the expelled mass thereby increasing its exhaust velocity. There are a number of different ways to supply this energy to the rocket, but the majority of conventional rockets use either chemical means or electrical means.

A chemical rocket provides energy to the system by utilizing the energy stored in the chemical bonds of the propellant. While in operation, these chemical bonds are broken through various chemical reactions. The kinetic energy in the system increases and this higher energy mass is subsequently directed out of the rocket by gasdynamic nozzles. These nozzles make sure to align the energetic flow along a common axis allowing there to be an opposite reaction in the desired direction of motion. Examples of chemical propulsion systems include monopropellants that use compounds such as hydrazine and hydrogen peroxide and bipropellants that use compounds such as oxygen–hydrogen and dinitrogen tetroxide–monomethylhydrazine[2]. Because chemical rockets are limited to the amount of energy stored in the propellants' chemical bonds, they are

characterized as energy-limited systems. The amounts of energy stored in these bonds are relatively small compared to energy stored by other atomic and molecular means, such as nuclear bonds and, therefore, limits the I_{sp} of chemical rockets to a maximum of about 450s.[2] However, because of the abundance of propellants used by chemical rockets, large amounts can be amassed and create as much as 5 MN or over one million pounds of thrust.[2]

An electric propulsion system uses an electrical power generator to add energy to the propellant. Power can be generated through various methods including solar photovoltaic, radioisotope, nuclear reactor, and fuel cells. Electric propulsion systems can be further categorized depending on the method by which the propellants gain energy. Electrostatic and electromagnetic classes of thrusters, including ion, Hall, and pulsed plasma thrusters, use electric and magnetic fields to impart energy to the propellant. The electrothermal class of thrusters, including arcjets, resistojets, and the MET, convert electrical energy to thermal energy, which accelerates the propellant through nozzles similar to that of chemical rockets. Electric propulsion systems are not limited by energy stored in the propellants but rather the amount of energy added to the propellants via the power source. This results in electric propulsion systems being characterized as power-limited systems and can reach I_{sp} values of 6000s[2]. However, there are losses associated with power transmission and consumption since not all of it will be used for propulsion. This efficiency, η_τ, can be calculated by[2]

$$\eta_\tau = \frac{P_\tau}{P_{\text{input}}} = \frac{\frac{1}{2}\dot{m}u_e^{\,2}}{P_{\text{input}}} \tag{1.6}$$

Rearranging Equation (1.6) and combining it with thrust, Equation (1.4), and specific impulse, Equation (1.5), an equation for the amount of power required for a certain thrust, specific impulse, and efficiency is[2]

$$P_{\text{input}} = \frac{gI_{sp}\tau}{2\eta_\tau} \tag{1.7}$$

It is interesting to note that at a constant power level and rocket efficiency, an increase in thrust requires a decrease in specific impulse, and a decrease in thrust results in an increase in specific impulse. These observations are a result of the amount of mass flow through the system. A higher mass flow results in an increase in thrust, but also a decrease in specific impulse. A tradeoff must be made and the amount of propellant used per time period will need to vary depending on the mission objectives.

1.2 Microwave Electrothermal Thruster Overview

The Microwave Electrothermal Thruster (MET) is a specific class of electrothermal propulsion system. It uses microwave energy to create coalesced plasma near the entrance to the gasdynamic nozzle. The propellant is swirled into the MET chamber and heated as it passes around the coalesced plasma. It is then exhausted through the nozzle and out of the system.

1.2.1 Fundamental Design and Operation

The structure of the MET mimics that of a circular cross section waveguide. It is specifically designed for the TM^{z}_{011} resonance mode at a certain frequency within the microwave spectrum, and is accomplished by precisely sizing the cavity height-to-diameter ratio. This resonance mode is chosen because it has strong electric field concentration at the ends of the cavity's central axis. This allows for the highest possible transfer of energy to the surrounding propellant. Figure 1.2 shows the MET cavity with the TM^{z}_{011} resonance mode field lines.

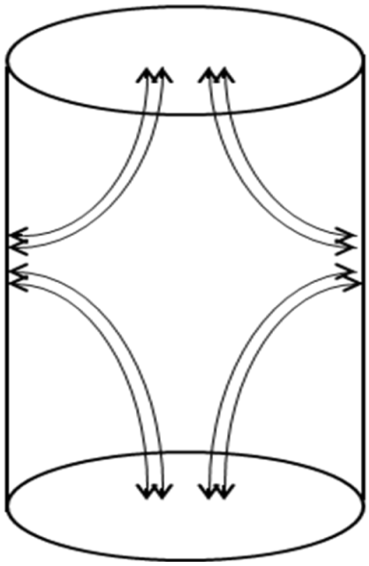

Figure 1.2 MET cavity with electric field lines for TM^{Z}_{011} resonance mode

The thruster itself is an aluminum block with a circular hole bored through its center, sized to resonate at a certain microwave frequency as described above. It is capped by two conductive endplates, a base plate and a nozzle plate, allowing for a short of the conductive aluminum chamber. The base plate contains an antenna by which the microwaves radiate into the MET cavity.

Propellant is injected into the chamber using a number of interchangeable injectors varied by diameter size. Coalesced plasma is forms in the highest electric field concentration near the nozzle. The propellant is injected tangentially, swirling through the chamber. This helps to stabilize the free-floating plasma along the center axis by creating a radial pressure gradient. The propellant is heated by the plasma and subsequently choked and exhausted through the gasdynamic nozzle.

There are two versions of the MET discussed in this thesis. The first version is a single, solid cavity such that the propellant and resulting chamber pressure is fairly consistent from base plate to nozzle plate. This chamber variation was unable to produce any viable experimental data. The high concentration of electric field at the antenna due to the symmetry of the TM^{z}_{011} mode also created a plasma, which ultimately damaged and destroyed the antenna despite the addition of a dielectric antenna cap. Because of this fact, a second version of the MET was created with a dielectric separation plate that

divided the chamber into two halves. The separation plate, composed of quartz or boron nitride, maintains atmospheric pressure within the antenna half of the chamber, while allowing for the required variance of pressure in the plasma half of the chamber. The antenna is protected because plasma cannot form at atmospheric (or higher) pressure at input powers of less than 350 W. A plasma can only ignite at the low pressure maintained in the plasma half of the cavity. Figure 1.3 shows both variations of the MET cavity.

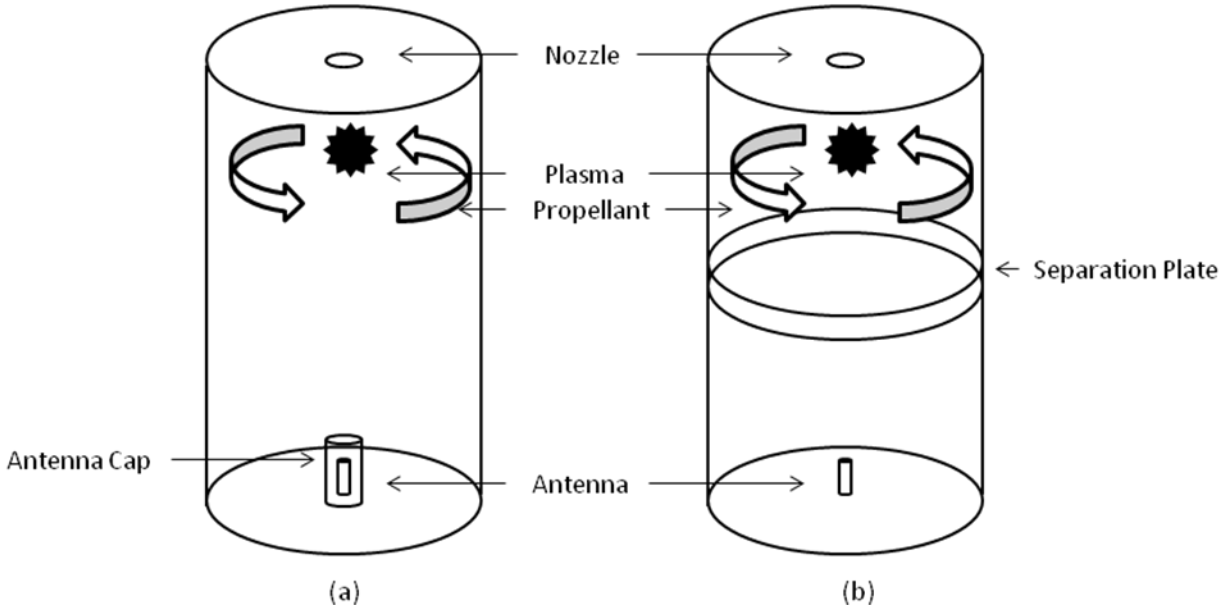

Figure 1.3 **(a) MET chamber version with a dielectric antenna cap; (b) MET chamber version with a separation plate**

1.2.2 Prior Research on the MET

Research on the MET has been conducted at The Pennsylvania State University since the mid 1980s. Studies by Balaam, Maul, and Micci[4,5] built upon previous lower power (maximum of 500 W) studies of the effectiveness of plasma discharge formations created from 2.45-GHz microwave sources in heating a propellant. A higher power model (maximum of 2500 W) was built and tested using helium and nitrogen propellants.

Sullivan and Micci[6] continued studying the characteristics of the MET by experimenting with alternative propellant gases, including hydrogen and ammonia.

Although these tests led to the failure of the quartz cavities due to higher temperatures, they still proved the viability of using these gases as effective heat transferring plasmas under the right thruster design and circumstances.

Research continued with Mueller[7] who experimented with using waveguide-heated plasmas. A rectangular waveguide chamber was used and a stable plasma with up to 90% coupling efficiency was created and sustained within a TE_{10} electromagnetic field pattern. However, thruster erosion and a decrease in efficiency resulted because of the interaction of the plasma with the rectangular resonant chamber walls. This led to the use of a circular resonant cavity where a stable plasma with up to 96% coupling efficiency was created without any interaction with the chamber's wall. Using helium propellant and a converging only nozzle, the specific impulse and thrust at 1000 W reached upwards of 350 s and 0.4 N, respectively.

Sullivan[8] began the development of a prototype thruster using data gathered from previous experiments and computational modeling. This included design features that position the plasma near the entrance to the nozzle and injected propellant gases tangentially, stabilizing the plasma. The propellant gases used were nitrogen, ammonia, hydrogen, and helium. The thruster operated at 2200 W in excess of two hours and had coupling efficiencies greater than 97% using nitrogen and ammonia as propellant.

Research continued with Kline[9] conducting thrust measurements of the 2.45-GHz MET operating at a lower power (815 W). A thrust stand was built in a pendulum arrangement and used gravity as the restoring force. A linear variable differential transformer (LVDT) measured the horizontal displacement of the thruster while in operation. The experiment used nitrogen as the propellant and achieved 54% efficiency, a specific power measurement of 7.8 MJ/kg, a specific impulse of 295 s, and thrust levels of 303 mN with a thrust stand accuracy of ± 10 mN.

Nordling[10] was the first to test a high frequency, low power version of the MET. The thruster was scaled down from a 2.45-GHz, kilowatt-class thruster, to a 7.5-GHz, 100 W variety. Initially, a suspended thrust stand similar to Kline's was used for thrust measurements, but it was too inaccurate to be used with the extremely low thrust-to-weight ratio of the new 7.5-GHz thruster. A new, inverted pendulum thrust stand was created for more accurate measurements above 2 mN with resolution of 0.333 mN.

Thrusts of 7.66 mN and 13.77 mN and specific impulses of 176.3 s and 130.9 s were measured for helium and nitrogen respectively. A 4% overall efficiency was achieved for both of these gases.

Souliez[11] continued MET research on both the 7.5-GHz and 2.45-GHz variations. Low power (<100 W) vacuum tests were performed on both thrusters and determined that at this power level, the 2.45-GHz thruster's chamber pressure was not high enough to produce enough thrust for realistic usage on a spacecraft. However, the 7.5-GHz thruster continued to provide results, producing thrusts of 21.44 mN and 19.4 mN and specific impulses of 178 s and 89 s for helium and nitrogen, respectively. It should be noted that higher mass flows resulted in higher thrust values for Souliez's experiment compared to Nordling's experiment for similar propellants and power levels.

While Nordling was able to produce useful data for MET research advancement, there were problems found using the inverted pendulum thrust stand when testing with nitrogen. One problem was that the coalesced plasma experienced buoyancy issues because of the weight of the cold nitrogen gas and the horizontal orientation of the thruster. This caused uneven heating of the nozzle entrance, leading to erosion and melting. Roos[12] used a new, vertically oriented thrust stand designed by Souliez *et al.*[13] to avoid this problem. The stand employed a beam-and-fulcrum design where the thruster was attached to one end and a counterweight was attached to the other. A LVDT was still used to measure displacement of the beam, but this time in the vertical direction. Inaccuracies of less than 0.5 mN were reported with a resolution of better than 1 mN. Using helium as the propellant, a thrust value of 19.95 mN and a specific impulse of 228 s were achieved with no more than 66 W of input power.

Welander[14] changed the method of thrust measurement altogether by mounting the MET on a fixed flange and exhausting the propellant into a vacuum environment, simulating space. On the vacuum side of the flange, a momentum trap was hung from a beam with a stain gage measuring the deflection of the beam. The momentum trap captured the exhausted propellant and imparted its momentum onto the beam. A calibration of the strain gage using known weights allowed measured deflections caused by the exhausted gases to be converted into thrust data. This method of thrust

measurement was previously used by Diamant, Cohen, and Brandenburg.[15] Initial testing was unsuccessful but laid the groundwork for future thrust measurements.

Clemens[16] continued the research of the low power, 7.5-GHz MET using the momentum trap described above as the thrust measurement device. Clemens performed nitrogen tests in a vacuum environment using three different types of nozzles. The momentum trap concept was verified with accurate cold flow measurements; however, once a plasma was lit, the heat transfer between the exhaust and momentum trap caused a thermal expansion of the thrust stand, leading to inaccurate thrust measurements. But Clemens was able to reach a maximum thrust of 20.8 mN and a specific impulse of 204 s using a 0.0107-inch-diameter converging–diverging tungsten nozzle and nitrogen propellant at an average of 63 W of input power.

In an effort to reduce the size and power consumption of an MET, a new version of the thruster was developed and tested by Goovaerts.[17] This new thruster is a 14.5-GHz scaled-down version of the MET with a maximum absorbed power of 20 W. The goal was to determine the feasibility of the thruster using helium gas as its propellant. This goal was achieved; however, significantly high chamber temperatures were not created and a theoretical thrust value of only 4.2 mN and a theoretical specific impulse of only 197 s were achieved. This prompted a redesign of the thruster, which is currently undergoing testing and verification.

Clemens[18] continued research on both the 7.5-GHz and 2.45-GHz MET. Nitrogen and for the first time simulated decomposition products of hydrazine were used as propellants in the 7.5-GHz MET. Other parametric studies including nozzle throat diameter, microwave frequency, and input power were conducted resulting in a maximum calculated specific impulse of 220 s. Parametric studies including effects of nozzle throat diameter, antenna probe depth, propellant injector diameter, and the inclusion of an impedance matching unit were performed on the 2.45-GHz thruster. Also, simulated hydrazine and pure ammonia were used as propellants. Maximum theoretical specific impulse values of 400 s for ammonia and 425 s for simulated hydrazine were calculated. However, thrust stand measurements using a momentum trap for the 7.5-GHz thruster and a similarly designed deflection cone and strain gauge system

for the 2.45-GHz thruster were only able to produce values 40% lower than those of the calculated values.

1.2.3 Motivation for an 8-GHz MET

The microwave electrothermal thruster, as discussed above, is classified as an electrothermal electric propulsion device, in that electricity is used to transfer heat to the propellant before it is exhausted out of a gasdynamic nozzle. One of the leading flight-capable electrothermal thrusters currently in operation is the arcjet thruster. This thruster utilizes an electric arc created between two electrodes to transfer heat to the propellant. The MET is being developed to compete with the arcjet and possibly replace it on future space missions The primary advantage of using an MET over an arcjet is that the MET uses a free-floating plasma to heat the propellant as opposed to the arcjet's electric arc. The MET's plasma does not come into contact with the thruster's hardware and, therefore, does not cause nearly the amount of erosion experienced by the arcjet's electrodes, leading to a longer lifetime of the thruster. This advantage, however, does not impede the performance of the MET as similar thrust levels and specific impulses are expected. Also, because the electrodes in an arcjet experience higher heat loss when creating an arc as compared to the heat lost during plasma formation in the MET cavity, an operational MET is predicted to operate at a higher overall efficiency than the arcjet.

Extensive research has already been performed on the 2.45-GHz and 7.5-GHz MET. The 2.45-GHz version requires approximately 1000 W of power in order to operate with any success. Conversely, the 7.5-GHz thruster has been tested at no more than 100 W of input power. However, the availability of a space-rated TWTA power supply had drawn some interest in a new intermediate-power MET. Clemens[18] designed the new MET around the 7.9 to 8.4-GHz operating specifications of the TWTA. The chamber was decreased in size slightly in order to accommodate the slightly higher frequency. The new 8-GHz chamber was also designed to operate at a maximum of 350 W, 250 W more than the 7.5-GHz MET. The higher frequency (smaller chamber) and higher power results in the 8-GHz MET having a higher energy density than the 2.45-

GHz and 7.5-GHz thrusters. This means that the new thruster can sustain a plasma at higher chamber pressures, allowing for better performance.

Preliminary testing of the 8-GHz MET was conducted by Clemens[18] using simulated hydrazine. Figures 1.4 through 1.7 show the results of this preliminary testing.

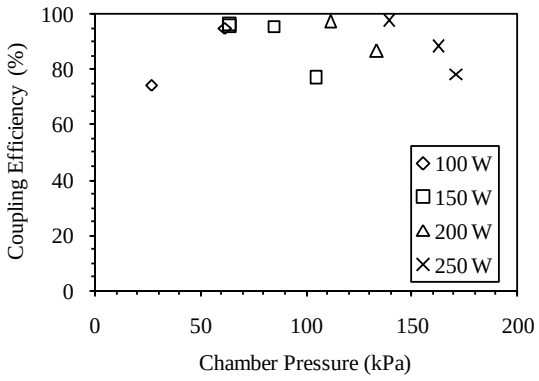

Figure 1.4 **Coupling efficiency vs. chamber pressure using simulated hydrazine. Forward power is given in legend. [ref. 18]**

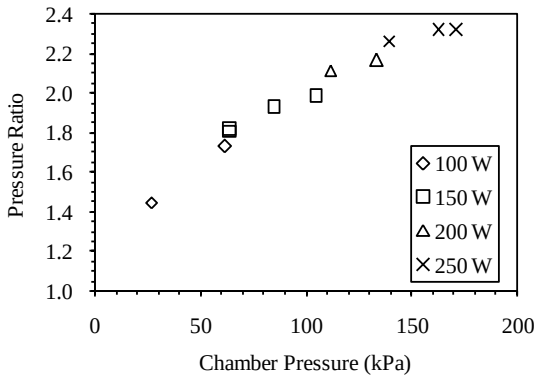

Figure 1.5 **Pressure ratio vs. chamber pressure using simulated hydrazine. Forward power is given in legend. [ref. 18]**

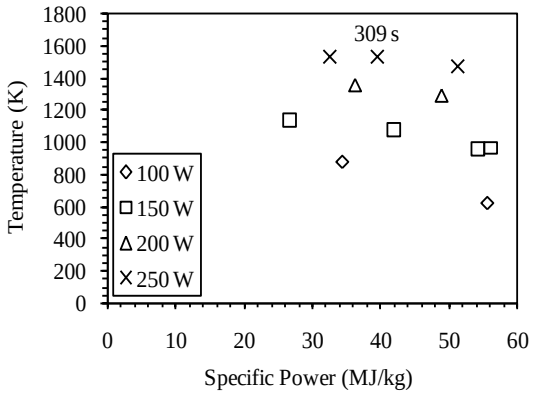

Figure 1.6 **Chamber temperature vs. specific power using simulated hydrazine. Forward power is given in legend. Maximum specific impulse is shown. [ref. 18]**

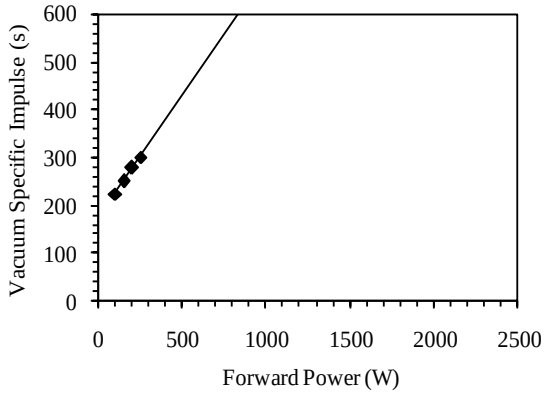

Figure 1.7 **Vacuum specific impulse vs. forward power using simulated hydrazine for operating conditions with ~95% coupling efficiency. [ref. 18]**

The cavity, in fact, did have a resonant frequency of 8.16-GHz as predicted by the computational and numerical modeling of the chamber. A coupling efficiency of over 95% was attained and was able to be maintained at higher mass flows by increasing the

input power. The maximum chamber pressure was 175 kPa, higher than both the 2.45-GHz and 7.5-GHz METs. However, the performance of the 8-GHz chamber did not exceed that of the 2.45-GHz, only reaching a maximum theoretical specific impulse of 309 s assuming perfect nozzle expansion. Figure 1.7 shows the calculated maximum specific impulse at incremental power levels. A trend line has been inserted, predicting that at higher powers, this new 8-GHz MET will outperform the 2.45-GHz MET at 500 W and ultimately outperform the arcjet at 1000 W, making it a true competitor among spacecraft propulsion systems.

1.2.4 Thesis Overview

This thesis will present the continued evaluation and optimization of the 8 GHz MET. The physical theory governing the operation of the 8-GHz MET is discussed in Chapter 2. The experimental setup and procedures are presented in Chapter 3. The experimental results are displayed in Chapter 4. Finally, Chapter 5 provides conclusions and recommendations for future testing based on the data obtained.

CHAPTER 2
Physical Theory

The mechanics of the MET consist of many different scientific laws and theories, all acting together for proper thruster operation. These include many theoretical models found in fluid mechanics, electromagnetics, thermodynamics, and some propulsion chemistry. Direct solutions to these models with regards to the MET are very complex and would take too much time to do by hand. Computers are able to find approximate solutions to these theoretical models, but experimental tests can confirm if these approximations are correct. An understanding of the different theoretical models must first be made in order to understand the results of the experimental tests or computational solutions.

2.1 Fluid Mechanics and Flow Characterization

Fluid dynamics and thermodynamics are the bases needed to analyze most forms of propulsion systems, including the MET. Understanding how the fluid moves and reacts through the system helps in explaining experimental results and predicting future system responses.

2.1.1 Governing Equations

The theories governing fluid mechanics are grounded in the most basic and general laws of nature, and are represented by the conservation equations. The first of these conservation equations is the continuity equation, which states that mass can be neither created nor destroyed.[3] The second conservation equation is the momentum equation which states the time rate of change of momentum of a body equals the net force exerted on it.[3] A variation of this equation, also known as Newton's Second Law, is presented in Chapter 1 of this thesis as Equation (1.1). The third conservation equation is the energy equation which states that energy can be neither created nor destroyed and can

only change form. This equation is also known as the first law of thermodynamics.[3] The governing continuity, momentum, and energy equations presented mathematically are

$$-\int_{CS} \rho \bar{v} \bullet d\bar{S} = \frac{d}{dt} \int_{CV} \rho dV \tag{2.1}$$

$$\int_{CS} (\rho \bar{v} \bullet d\bar{S}) \bar{v} + \int_{CV} \frac{d(\rho \bar{v})}{dt} dV = \int_{CV} \rho \bar{f} dV - \int_{CS} p d\bar{S} \tag{2.2}$$

$$\int_{CV} \dot{q} \rho dV - \int_{CS} p \bar{v} \bullet d\bar{S} + \int_{CV} \rho (\bar{f} \bullet \bar{v}) dV = \int_{CV} \frac{d}{dt} \left[\rho \left(e + \frac{v^2}{2} \right) \right] dV + \int_{CS} \rho \left(e + \frac{v^2}{2} \right) \bar{v} \bullet d\bar{S} \tag{2.3}$$

These conservation equations are very complex in their general form, but assumptions that apply to MET propulsion system can be made to simplify them into more workable equations. These assumptions are steady, one dimensional, compressible flow. Enthalpy, *h*, is the product of pressure and specific volume, *pv*, summed with internal energy, *e*. The combination of these assumptions, the definition of enthalpy, and some algebraic manipulation results in the simplified continuity, momentum, and energy conservation equations[3]

$$\rho_1 u_1 A_1 = \rho_2 u_2 A_2 \tag{2.4}$$

$$p_1 A_1 + \rho_1 u_1^2 A_1 + \sum F = p_2 A_2 + \rho_2 u_2^2 A_2 \tag{2.5}$$

$$h_1 + \frac{u_1^2}{2} + q = h_2 + \frac{u_2^2}{2} \tag{2.6}$$

2.1.2 Thermodynamics

The thermodynamic properties of a specific fluid are derived from the two laws of thermodynamics. The first law, as described above, explains that energy is conserved, in that it cannot be created nor destroyed. A simplified, per unit mass differential form of the first law is

$$dq = de + dw \tag{2.7}$$

The second law explains that as a system proceeds through a process, there are losses associated with the process and the system cannot return to its original form. The second law also introduces a variable called entropy, *s*, which helps to describe the losses associated with various processes. Entropy is defined as[1]

$$ds \geq \frac{dq}{T} \tag{2.8}$$

By introducing a reversible process that defines *dw* from Equation (2.7) as *pdv*, Equation (2.7) and Equation (2.8) are combined to form[1]

$$Tds = de + pdv \tag{2.9}$$

The propellant used by the MET can be accurately approximated by assuming they are ideal gases. The ideal gas law is a convenient equation of state that creates a relationship between many physical states of the gases and is expressed as

$$P = \rho RT \tag{2.10}$$

Combining the definition of enthalpy, $h = e + pv$, the definition of specific heat at constant pressure, $c_p = dh/dT$, the definition of specific heat at constant volume,

$c_v = de/dT$, Equation (2.9), Equation (2.10), and the relation that $c_p - c_v = R$ results in the following relationship[1]

$$ds = c_p \frac{dT}{T} - R\frac{dp}{p} \tag{2.11}$$

2.1.3 Isentropic Flow

Another useful approximation is to assume that the hot fluid flow from the chamber to the exit of the nozzle is isentropic. Isentropic flow indicates that the flow is reversible, no change in entropy, and adiabatic, no heat transfer to or from the fluid. The isentropic assumption is applied to Equation (2.11) by setting *ds* equal to zero. This new equation is integrated and the relationship $c_p/c_v = \gamma$ is used to create the relationship between pressure and temperature[1]

$$\frac{p_0}{p} = \left(\frac{T_0}{T}\right)^{\frac{\gamma}{\gamma-1}} \tag{2.12}$$

A combination of Equation (2.12) and the ideal gas law, Equation (2.10), results in

$$\frac{p_0}{p} = \left(\frac{\rho_0}{\rho}\right)^{\gamma} \tag{2.13}$$

$$\frac{\rho_0}{\rho} = \left(\frac{T_0}{T}\right)^{\frac{1}{\gamma-1}} \tag{2.14}$$

The isentropic assumption introduces a stagnation state of the fluid. This state is defined as the state of a fluid that is brought to rest isentropically and without work.[1] The stagnation or total state is designated by the subscript 0, as can be seen in Equations (2.12) through (2.14). The stagnation state is easily measured in the chamber of the

MET, where the speed of the fluid is very low compared to the flow through the nozzle. This state and the isentropic assumption are useful for predicting the performance of MET by using the theory developed later in this chapter.

The energy equation, Equation (2.6), can be used to define the total enthalpy at the stagnation state, $h_0 = h + u^2/2$. The combination of total enthalpy and the definition of specific heat at constant pressure is

$$\frac{T_0}{T} = 1 + \frac{u^2}{2c_p T} \tag{2.15}$$

Because the fluid is moving with speeds varying from subsonic to supersonic, a convenient variable called the Mach number is established. It is defined as the ratio of the speed of the fluid to the local speed of sound of the fluid. The Mach number is expressed as

$$M = \frac{u}{\sqrt{\gamma RT}} \tag{2.16}$$

By using the relationship $c_p = \gamma/(\gamma - 1)R$ in combination with Equations (2.15) and (2.16), a relationship between the local temperature, total temperature, and speed of the fluid is created and expressed as

$$\frac{T_0}{T} = 1 + \frac{\gamma - 1}{2} M^2 \tag{2.17}$$

A relationship between the local and total pressures and the fluid speed is created by combining Equation (2.17) with Equation (2.12), which is expressed as

$$\frac{p_0}{p} = \left(1 + \frac{\gamma - 1}{2} M^2\right)^{\frac{\gamma}{\gamma - 1}} \tag{2.18}$$

A relationship between the local and total densities and the fluid speed is created by combining Equation (2.17) with Equation (2.14), which is expressed as

$$\frac{\rho_0}{\rho} = \left(1 + \frac{\gamma - 1}{2} M^2\right)^{\frac{1}{\gamma - 1}} \tag{2.19}$$

These three equations, Equations (2.17)–(2.19), are known as the isentropic flow equations.[1]

2.1.4 Performance Analysis Equations

The theory developed above, especially the isentropic flow equations, are used for deriving equations that are useful in predicting flow characteristics throughout a gas dynamic propulsion system. These derivations start with a variation of the continuity equation,

$$\dot{m} = \rho u A \tag{2.20}$$

The combination of this form of the continuity equation, the isentropic flow equations, and the equation defining the Mach number results in a useful equation for mass flow,

$$\dot{m} = \frac{A p_0 \sqrt{\gamma}}{\sqrt{R T_0}} M \left(\frac{1}{1 + \frac{\gamma - 1}{2} M^2}\right)^{\frac{(\gamma+1)}{2(\gamma-1)}} \tag{2.21}$$

Remember that flow through the chamber portion of the system is very slow compared to the rest of the system and can be approximated as zero. This means that the stagnation conditions and chamber conditions are one in the same and henceforth will be referred to as chamber conditions, denoted by a subscript *c* instead of a subscript 0.

In a gas dynamic nozzle, the fluid conditions at the throat are said to be choked and cannot flow faster than the speed of sound. The characteristics of the fluid choked at the throat of the nozzle will be indicated with an asterisk and the Mach number will always be equal to one. The mass flow equation above, Equation (2.21), applied to the throat of the nozzle simplifies to

$$\dot{m}^* = \frac{A^* p_c \sqrt{\gamma}}{\sqrt{RT_c}} \left(\frac{2}{\gamma + 1} \right)^{\frac{(\gamma+1)}{2(\gamma-1)}} \tag{2.22}$$

Recall that one of the assumptions made at the beginning of this chapter is that there is steady flow through the nozzle. This means that all mass flow through the system must be equal, regardless of location. Equating Equations (2.21) and (2.22) along with some algebraic manipulation creates an expression useful for calculating cross-sectional area ratios for specific system conditions and requirements,

$$\frac{A}{A^*} = \frac{1}{M} \left[\frac{2}{\gamma + 1} \left(1 + \frac{\gamma - 1}{2} M^2 \right) \right]^{\frac{(\gamma+1)}{2(\gamma-1)}} \tag{2.23}$$

This equation is most useful when applied to the exit of the nozzle. An exit Mach number can be calculated using the ratio of nozzle exit area and throat area. However, it is also useful to derive the flow's exit velocity in terms of flow characteristics.

This derivation begins with the energy equation, Equation (2.6), and is expressed in terms of the system's chamber and exit locations. Note that the processes occurring between the chamber and exit are adiabatic processes and therefore the heat transfer is zero. This system's specific energy equation is expressed as

$$h_c + \frac{u_c^2}{2} = h_e + \frac{u_e^2}{2} \tag{2.24}$$

Once again, recall that chamber velocity is essentially equal to zero. Using the definition of enthalpy, Equation (2.24) can then be expressed as

$$\frac{u_e^2}{2} = h_c - h_e = c_p\left(T_c - T_e\right) \tag{2.25}$$

A combination of Equation (2.25) with the isentropic relation expressed in Equation (2.12), the equation relating c_p with γ and R, $c_p = \gamma/(\gamma - 1)R$, yields an equation for exit velocity,

$$u_e = \sqrt{\frac{2\gamma R}{(\gamma - 1)} T_c \left[1 - \left(\frac{p_e}{p_c}\right)^{\frac{(\gamma-1)}{\gamma}}\right]} \tag{2.26}$$

The momentum equation derived in the beginning of this chapter, Equation (2.5) is used to derive the thrust equation as described in Chapter 1,

$$\tau = \dot{m} u_e + (p_e - p_a) A_e \tag{2.27}$$

Substituting Equation (2.22) and (2.26) into Equation (2.27) yields a variation of the thrust equation,

$$\tau = p_c A^* \sqrt{\frac{2\gamma^2}{\gamma - 1}\left(\frac{2}{\gamma + 1}\right)^{\frac{\gamma+1}{\gamma-1}} \left[1 - \left(\frac{p_e}{p_c}\right)^{\frac{\gamma-1}{\gamma}}\right]} + \left(p_e - p_a\right) A_e \tag{2.28}$$

It is sometimes convenient to analyze the performance of the propulsion system by dividing the system into two parts, the chamber and the nozzle, and evaluating them separately.

The chamber's specific performance evaluation parameter is called the characteristic velocity, c^*. The characteristic velocity is only a function of the chamber conditions and throat area, expressed as

$$c^* = \frac{p_c A^*}{\dot{m}} \tag{2.29}$$

Substituting Equation (2.22) into Equation (2.29), produces a variation of the characteristic velocity equation,

$$c^* = \sqrt{\frac{1}{\gamma}\left(\frac{\gamma+1}{2}\right)^{\frac{\gamma+1}{\gamma-1}} RT_c} \tag{2.30}$$

The nozzle's specific performance evaluation coefficient is called the thrust coefficient, C_τ. The thrust coefficient is a function of the nozzle geometry as well as stagnation pressure and is expressed as

$$C_\tau = \frac{\tau}{p_c A^*} \tag{2.31}$$

Substituting Equation (2.28) into Equation (2.31), yields a variation of the characteristic velocity equation,

$$C_\tau = \sqrt{\frac{2\gamma^2}{\gamma-1}\left(\frac{2}{\gamma+1}\right)^{\frac{\gamma+1}{\gamma-1}}\left[1-\left(\frac{p_e}{p_c}\right)^{\frac{\gamma-1}{\gamma}}\right]} + \frac{p_e - p_a}{p_c}\frac{A_e}{A^*} \tag{2.32}$$

A convenient expression for thrust is derived when combining Equations (2.29) and (2.31) in terms of characteristic velocity, thrust coefficient, and mass flow as[1]

$$\tau = \dot{m} C_\tau c^* \tag{2.33}$$

2.1.5 Discharge Coefficient and Boundary Layer Losses

In fluid dynamics, frictional losses are mostly prevalent near the boundary along which the fluid is flowing. Whether a no slip or slip condition is assumed, a boundary layer is created because of a significant slowing of fluid next to the surface. The boundary layer becomes more exaggerated as the cross sectional area of the orifice, in this case the nozzle, becomes smaller. This is because the boundary layer's height is a higher percent of the cross sectional diameter as the nozzle's area decreases. In effect, this phenomenon reduces the cross sectional area of the nozzle, restricting the amount of fluid through the nozzle. This results in a decrease in thruster performance. The MET's nozzles are small enough to be affected by this boundary layer loss; therefore it must be considered when calculating performance.

The factor by which the performance calculation equations are corrected for the boundary layer loss is called the discharge coefficient, C_d. It is defined as the ratio of actual measured mass flow to the theoretical mass flow. It is incorporated into Equation (2.22) and subsequently solved for, yielding

$$C_d = \frac{\dot{m}_{\text{actual}}}{\frac{A^* p_c \sqrt{\gamma}}{\sqrt{RT_c}} \left(\frac{2}{\gamma + 1} \right)^{\frac{(\gamma+1)}{2(\gamma-1)}}} \tag{2.34}$$

The discharge coefficient is related to the boundary layer effect of the nozzle, as stated above. Boundary layers, however, are consequences of the Reynolds number of the fluid. The Reynolds number based on nozzle throat diameter is

$$R_e = \frac{\rho^* u^* d^*}{\mu^*} \tag{2.35}$$

These conclusions lead to the assumption that the discharge coefficient and Reynolds number are dependent on each other. However, because the Reynolds number is a function of the temperature dependent viscosity, the discharge coefficient is dependent on temperature. Equation (2.34) then cannot be used to directly solve for chamber temperature because of the discharge coefficient's dependence on temperature. Instead, a more indirect method must be used to determine the discharge coefficient and chamber temperature, assuming fluid specific heats are known.

Using cold flow pressure and mass flow measurements, the Reynolds number and discharge coefficient can be calculated and plotted against each other. Also, a relationship between temperature and viscosity can be determined using published data sources. These relationships, along with the Reynolds number equation, discharge coefficient equation, and the isentropic flow equation in terms of temperature, can be solved simultaneously to find the chamber temperature and discharge coefficient. The more accurate effective throat area is a result of the product of the discharge coefficient and known throat area. The performance calculations of the thruster can now be corrected for nozzle boundary layer effects.

2.2 Electromagnetic Theory

As described in Chapter 1, the MET is categorized as an electric propulsion device. Microwave energy is transmitted into the MET and is subsequently imparted to the swirling propellant gas, allowing for thruster operation. The behavior of the microwave signal throughout the MET is governed by electromagnetic theory. In this section, the derivation of the electromagnetics that apply to the system is divided into three sections. The first section discusses the theory of power delivery through a rectangular waveguide system, developed using Maxwell's field equations. The second section is a discussion of transmission line theory, developed using Kirchhoff's circuit theory. The third section is a discussion about electromagnetic resonance in the thruster, developed using Maxwell's field equations.

2.2.1 Waveguide Signal Propagation

The wavelength at which the 8-GHz MET operates is about 3.75 cm and is the same order of magnitude of a reasonably sized circuit. This allows for a unique method by which the microwave signal can be transmitted to the thruster chamber. This method uses a network of hollow tubes called waveguides to propagate the signal, instead of using less efficient cables and wires. The MET specifically uses WR112 rectangular waveguides sized to propagate 8-GHz microwave signals from the power source to the thruster chamber. Basic waveguide theory is discussed below; however, a more in depth derivation can be found in Pozar.[19]

Rectangular waveguides are governed by Maxwell's field equations, specifically the phasor forms of the curl equations,

$$\nabla \times \bar{E} = -j\omega\mu\bar{H} \tag{2.36}$$

$$\nabla \times \bar{H} = j\omega\varepsilon\bar{E} \tag{2.37}$$

where the values μ and ε are the permeability and permittivity respectively of the medium in the waveguide. These equations are expanded into their differential forms and simplified to a system of four equations. Assuming that the direction of propagation is in the *z* direction, these four equations are arranged such that the *x* and *y* components of the electric and magnetic fields are in terms of the *z* components of the electric and magnetic fields.

Waveguide systems are able to propagate both transverse electric (TE) and transverse magnetic (TM) waves. However, the wave propagation mode used by the MET waveguide system is the TE wave. The definition of the TE wave implies that the electric field in the direction of propagation (*z* direction) is equal to zero. This simplifies the four equations discussed before such that the *x* and *y* components of the electric and magnetic fields are only in terms of the *z* component of the magnetic field.

Using the Helmholtz wave equation in terms of the magnetic field,

$$\nabla^2 \overline{H} + \omega^2 \mu \varepsilon \overline{H} = 0 \tag{2.38}$$

which is also derived from Equations (2.36) and (2.37), and boundary conditions based on the geometry of the rectangular waveguide, a solution for the magnetic field in the *z* direction is calculated,

$$H_z = A_{mn} \cos \frac{m\pi x}{a} \cos \frac{n\pi y}{b} e^{-j\beta z} \tag{2.39}$$

where β is the phase constant, A_{mn} is the amplitude constant, and *a* and *b* are the width and height of rectangular waveguide section respectively. Substituting this solution into the four equations discussed above produces a field profile for a TE wave propagating through a rectangular waveguide. The dominant mode and mode of interest for a TE wave is the TE_{10} mode, whose field profile is

$$E_x = E_z = 0 \tag{2.40}$$

$$E_y = \frac{-j\omega\mu a}{\pi} A_{10} \sin \frac{\pi x}{a} e^{-j\beta z} \tag{2.41}$$

$$H_x = \frac{j\beta a}{\pi} A_{10} \sin \frac{\pi x}{a} e^{-j\beta z} \tag{2.42}$$

$$H_y = 0 \tag{2.43}$$

$$H_z = A_{10} \cos \frac{\pi x}{a} e^{-j\beta z} \tag{2.44}$$

The purpose of the waveguide system is to provide the power necessary for MET operation. Therefore, the power transmitted by a rectangular waveguide operating in the TE mode is calculated from the power equation

$$P = \frac{1}{2}\int_{CS} \bar{E} \times \bar{H}^* \bullet d\bar{S} = \frac{1}{2}\mathrm{Re}\int_{x=0}^{a}\int_{y=0}^{b} \bar{E} \times \bar{H}^* \bullet \hat{z}dydx \tag{2.45}$$

Substituting the field profile derived for the TE_{10} mode yields the power transmitted by the waveguide in the TE_{10} operating mode,

$$P_{10} = \frac{\omega\mu a^3 |A_{10}|^2 b}{4\pi^2}\mathrm{Re}(\beta) \tag{2.46}$$

Even though the microwave signal is mostly transmitted using a rectangular waveguide system, it does not enter the MET cavity via a rectangular waveguide. Instead, the signal is transitioned from a rectangular waveguide delivery system to a coaxial delivery system and enters the chamber via the coaxial line. The coaxial line signal propagation system is governed by transmission line theory.

2.2.2 Terminated Lossless Transmission Lines

Transmission line theory can be developed using either field or circuit theory and may be considered to be the connection between these two areas of study. The derivation presented is built from circuit theory.[19]

A transmission line is drawn as a two wire line because of the presence of at least two conductors. It can also be presented schematically using a lumped-element circuit. These two versions can be seen in Figure 2.1 below.

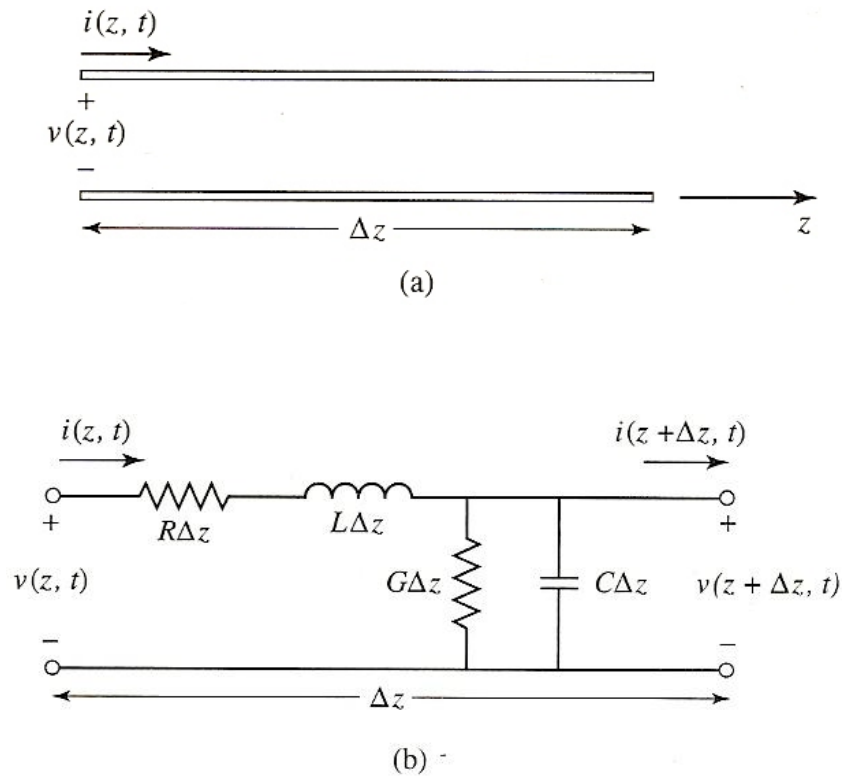

Figure 2.1 **Voltage and current definitions and equivalent circuit for and incremental length of transmission line. (a) Voltage and current definitions. (b) Lumped-element equivalent circuit. [ref. 19]**

Kirchhoff's Voltage Law, which states that the sum of the directed voltages around a closed circuit must be zero, and Kirchhoff's Current Law, which states that the sum of currents flowing towards a point in the circuit must be equal to the sum of current flowing away from that point, are used to summarize the circuit shown in Figure 2.1b and are expressed respectively as

$$v(z,t) - R\Delta z i(z,t) - L\Delta z \frac{\partial i(z,t)}{\partial t} - v(z+\Delta z,t) = 0 \tag{2.47}$$

$$i(z,t) - G\Delta z v(z+\Delta z,t) - C\Delta z \frac{\partial v(z+\Delta z,t)}{\partial t} - i(z+\Delta z,t) = 0 \tag{2.48}$$

Taking the limit as change in position, Δz, goes to zero, algebraic manipulation of these equations, and simultaneous substitutions produce wave equations for the voltage and current along the transmission line,

$$\frac{d^2V(z)}{dz^2} - \gamma^2 V(z) = 0 \tag{2.49}$$

$$\frac{d^2I(z)}{dz^2} - \gamma^2 I(z) = 0 \tag{2.50}$$

The complex propagation constant, γ, is expressed as

$$\gamma = \alpha + j\beta = \sqrt{(R + j\omega L)(G + j\omega C)} \tag{2.51}$$

As is the case with most practical applications, the transmission line used to propagate the microwave signal to the MET is assumed to be lossless, allowing for a simplification of the complex propagation constant. The series resistance in the line, *R*, and the shunt conductance between the two conductive sides of the line, *G*, are terms associated with losses and are subsequently both set to zero, leaving only the series inductance, *L*, and the shunt capacitance, *C*.

Equations (2.49) and (2.50) in conjunction with the lossless assumption provide traveling wave solutions for the voltages and currents along the transmission line,

$$V(z) = V_0^+ e^{-j\beta z} + V_0^- e^{j\beta z} \tag{2.52}$$

$$I(z) = I_0^+ e^{-j\beta z} + I_0^- e^{j\beta z} \tag{2.53}$$

In both equations, the term $e^{-j\beta z}$ describes the propagation of the wave in the positive *z* direction and the term $e^{j\beta z}$ describes the propagation of the wave in the negative *z* direction.

The characteristic impedance of the line, Z_0, is an important term in the development of transmission line theory. It is defined as the complex ratio of voltage to current in the line. The two terms that characterize the impedance are the real term R, which is the resistance in the line, and the complex term X, which is the reactance in the line. These definitions are

$$Z_0 = R + jX = \frac{V_0^+}{I_0^+} = -\frac{V_0^-}{I_0^-} \tag{2.54}$$

This definition allows Equation (2.53) to be rewritten as

$$I(z) = \frac{V_0^+}{Z_0} e^{-j\beta z} - \frac{V_0^-}{Z_0} e^{j\beta z} \tag{2.55}$$

The derivation of transmission line theory up to this point has assumed an infinite line. However, the transmission line as it is applied to the MET experiment is not infinite but terminated in the thruster. For the purpose of this derivation, the transmission line is terminated into an arbitrary load with impedance Z_L. Figure 2.2 shows a schematic of this terminated transmission line. Note that the origin for the distance coordinates is the load, with distance becoming more negative traveling left.

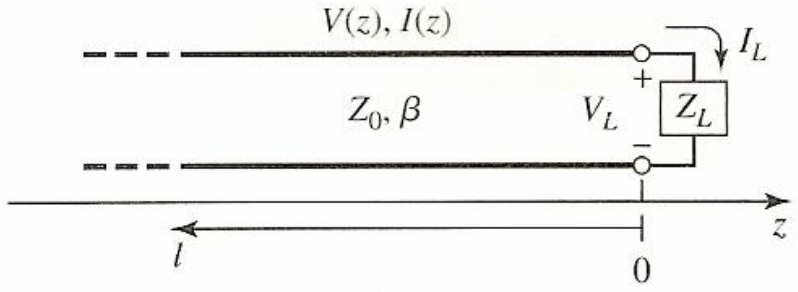

Figure 2.2 A transmission line terminated in a load impedance Z_L. [ref. 19]

Incident waves are produced from a source at $z < 0$ having the form $V_0^+ e^{-j\beta z}$ with characteristic impedance Z_0, as seen above. Assuming that $Z_0 \neq Z_L$, a reflected wave of the form $V_0^- e^{j\beta z}$ must be produced to satisfy the ratio of voltage to current caused by the mismatch. The incident and reflected wave are summed and have the same form as Equation (2.52). Through similar reasoning, the current on the line has the same form as Equation (2.55).

At the origin ($z = 0$), the voltage and current along the line are related to the load impedance, Z_L, and is expressed as

$$Z_L = \frac{V(0)}{I(0)} = \frac{V_0^+ + V_0^-}{V_0^+ - V_0^-} Z_0 \tag{2.56}$$

Solving this equation for V_0^- / V_0^+ produces the ratio of the reflected wave amplitude to the incident wave amplitude, which is known as the voltage reflection coefficient, Γ, and is expressed as

$$\Gamma = \frac{V_0^-}{V_o^+} = \frac{Z_L - Z_0}{Z_L + Z_0} \tag{2.57}$$

Equations (2.52) and (2.55) can now be rewritten as

$$V(z) = V_0^+ \left(e^{-j\beta z} + \Gamma e^{j\beta z} \right) \tag{2.58}$$

$$I(z) = \frac{V_0^+}{Z_0} \left(e^{-j\beta z} - \Gamma e^{j\beta z} \right) \tag{2.59}$$

The voltage and current on the line are now expressed as the superposition of an incident and reflected wave, which is known as a standing wave. It is interesting to note that when the characteristic impedance of the line, Z_0, is equal to the arbitrary load impedance, Z_L, Equation (2.57), namely the voltage reflection coefficient, Γ, becomes

zero. Reevaluating Equations (2.58) and (2.59) using this parameter results in an absence of reflected waves and the load is said to be matched to the line.

The overall interest in transmission line theory as it pertains to the MET results from the method by which power is supplied to the chamber. A relationship between the voltage and current along the transmission line and the average power anywhere along the line is expressed as

$$P_{\text{av}} = \frac{1}{2}\text{Re}\left[V(z)I^{*}(z)\right] \tag{2.60}$$

Combining Equations (2.58) through (2.60) results in

$$P_{\text{av}} = \frac{\left|V_0^{+}\right|^2}{2Z_0} - \frac{\left|V_0^{+}\right|^2}{2Z_0}\left|\Gamma\right|^2 \tag{2.61}$$

This equation shows that the total power imparted to (absorbed by) the load is the reflected power subtracted from the incident (forward) power. A simpler way of expressing Equation (2.61) is

$$P_{\text{av}} = P_{\text{abs}} = P_{\text{for}} - P_{\text{ref}} \tag{2.62}$$

A closer examination of Equations (2.61) and (2.62) show that if the voltage reflection coefficient is equal to zero, that is the transmission line and arbitrary load are matched, then there is no reflected power, allowing all of the power to be absorbed by the load. This derivation of transmission line theory reaches an interesting conclusion as it relates to the MET. If the impedance of the line is matched to the impedance of the chamber at its resonant frequency, then the maximum amount of power will be absorbed by the plasma.

2.2.3 TM^{z}_{011} Resonant Mode

The electromagnetic field that resonates in the MET depends greatly on the geometry of the cavity. Not only is the primary shape important (i.e. rectangular, cylindrical, spherical, etc.), but the dimensions of the cavity can greatly alter which resonance mode of the electromagnetic field will appear. The following derivation will describe the basic resonant cavity field theory that is applied to the 8-GHz MET cavity. The derivation will assume that the cavity is a perfect conductor that is filled with a homogeneous, lossless, source-free medium.

The shape of the MET's resonant cavity is that of a closed cylinder. Because of this, it is more efficient to derive the theory using a cylindrical coordinate system. Figure 2.3 shows this coordinate system as it applies to a cylindrical cavity.

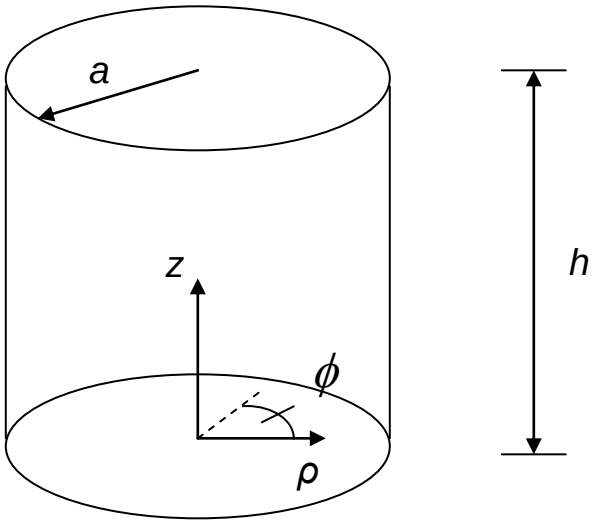

Figure 2.3 Cylindrical coordinate system of resonant cavity with radius *a* and height *h*.

The desired category of electromagnetic mode used in the MET is the transverse magnetic modes propagating in the positive *z* direction, abbreviated as TM^{z}. The reason for the selection of the specific TM^{z} mode (TM^{z}_{011}) is described in Chapter 1. Using the foundations of time harmonic EM field theory and a second-order differential equation

arrangement of Maxwell's equations, the electric and magnetic field components of the TM^z modes in cylindrical coordinates are

$$E_\rho = -j\frac{1}{\omega\mu\varepsilon}\frac{\partial^2 A_z}{\partial\rho\partial z} \tag{2.63}$$

$$E_\phi = -j\frac{1}{\omega\mu\varepsilon}\frac{1}{\rho}\frac{\partial^2 A_z}{\partial\phi\partial z} \tag{2.64}$$

$$E_z = -j\frac{1}{\omega\mu\varepsilon}\left(\frac{\partial^2}{\partial z^2}+\beta^2\right)A_z \tag{2.65}$$

$$H_\rho = \frac{1}{\mu}\frac{1}{\rho}\frac{\partial A_z}{\partial\phi} \tag{2.66}$$

$$H_\phi = -\frac{1}{\mu}\frac{\partial A_z}{\partial\rho} \tag{2.67}$$

$$H_z = 0 \tag{2.68}$$

The derivation of these components, as well as the vector potential presented below are far too long and time consuming to be presented in this thesis but can be found in Balanis.[20]

The vector potential, A_z, for the TM^z modes, is derived from a solution to the vector wave equation using cylindrical coordinates,

$$\nabla^2 A_z(\rho,\phi,z)+\beta^2 A_z(\rho,\phi,z)=0 \tag{2.69}$$

This solution is

$$A_z = B_{mn} J_m(\beta_\rho \rho)[C_2 \cos(m\phi) + D_2 \sin(m\phi)] \times [C_3 \cos(\beta_z z) + D_3 \sin(\beta_z z)] \quad (2.70)$$

where β is the phase constant and is defined as

$$\beta^2 = \beta_\rho^2 + \beta_z^2 = \omega^2 \mu\varepsilon \quad (2.71)$$

Tangential components of the electric field do not exist on conducting material surfaces. This fact produces a number of boundary conditions useful for further derivation of the cylindrical cavity's TM^z modes. These boundary conditions are

$$E_\rho(\rho, \phi, z = 0, h) = 0 \quad (2.72)$$

$$E_\phi(\rho, \phi, z = 0, h) = 0 \quad (2.73)$$

$$E_\phi(\rho = a, \phi, z) = 0 \quad (2.74)$$

$$E_z(\rho = a, \phi, z) = 0 \quad (2.75)$$

The electric field in the ϕ direction is obtained by combining Equations (2.64) and (2.70), yielding

$$E_\phi = -jB_{mn} \frac{m\beta_z}{\omega\mu\varepsilon} \frac{1}{\rho} J_m(\beta_\rho \rho)[-C_2 \sin(m\phi) + D_2 \cos(m\phi)] \times [-C_3 \sin(\beta_z z) + D_3 \cos(\beta_z z)] \quad (2.76)$$

The application of the boundary condition stated in Equation (2.74) sets Equation (2.76) equal to zero and ρ equal to a, resulting in a simplified equation,

$$J_m(\beta_\rho a) = 0 \tag{2.77}$$

This equation represents the Bessel function of the first kind. The solution to this function is

$$\beta_\rho a = \chi_{mn} \rightarrow \beta_\rho = \frac{\chi_{mn}}{a} \tag{2.78}$$

where χ_{mn} are zeroes of the Bessel function.

The application of the boundary condition stated in Equation (2.73) sets Equation (2.76) equal to zero and z equal to zero. Simplifying this new equation results in the constant D_3 equaling zero. Using the same boundary condition, but this time setting z equal to h, results in the simplification

$$\sin(\beta_z h) = 0 \tag{2.79}$$

The solution to this equation is

$$\beta_z h = p\pi \rightarrow \beta_z = \frac{p\pi}{h} \tag{2.80}$$

Substituting Equations (2.78) and (2.80) into Equation (2.71) and solving for the frequency term results in an equation useful for determining the resonant frequency of a cylindrical cavity with height h and radius a for a TM^z_{mnp} mode, expressed as

$$\left(f_{\mathrm{res}}\right)^{TM^z}_{mnp} = \frac{1}{2\pi\sqrt{\mu\varepsilon}}\sqrt{\left(\frac{\chi_{mn}}{a}\right)^2 + \left(\frac{p\pi}{h}\right)^2} \tag{2.81}$$

In particular, the desired TM^z resonance mode used for the MET is TM^z_{011}. Expressing all of the remaining constants as B_{mnp} and substituting these parameters into

the derived equations results in equations for the components of the electric and magnetic fields, as well as the resonant frequency for a given cavity height and radius. These are[16]

$$E_\rho = j\frac{B_{011}}{\omega\mu\varepsilon}\frac{\chi_{01}}{a}\frac{\pi}{h}J_o'\left(\frac{\chi_{01}}{a}\rho\right)\sin\left(\frac{\pi}{h}z\right) \tag{2.82}$$

$$E_\phi = 0 \tag{2.83}$$

$$E_z = -j\frac{B_{011}}{\omega\mu\varepsilon}\left(\frac{\chi_{01}}{a}\right)^2 J_o\left(\frac{\chi_{01}}{a}\rho\right)\cos\left(\frac{\pi}{h}z\right) \tag{2.84}$$

$$H_\rho = 0 \tag{2.85}$$

$$H_\phi = -\frac{B_{011}}{\mu}\frac{\chi_{01}}{a}J_o'\left(\frac{\chi_{01}}{a}\rho\right)\cos\left(\frac{\pi}{h}z\right) \tag{2.86}$$

$$H_z = 0 \tag{2.87}$$

$$\left(f_{\text{res}}\right)_{011}^{TM^z} = \frac{1}{2\pi\sqrt{\mu\varepsilon}}\sqrt{\left(\frac{\chi_{01}}{a}\right)^2 + \left(\frac{\pi}{h}\right)^2} \tag{2.88}$$

It should be noted that the frequency calculated using Equation (2.88) for the TM_{011}^{z} resonance mode only considers a cavity with the specific assumptions defined above. The frequency, however, can vary depending on the medium in the cavity, dielectric inserts, geometric irregularities in the cavity, and temperature increases and the plasma itself. The sizing of the cavity for the purposes of the MET must take these variables into account.

An important parameter involving resonance field theory is the quality factor, *Q*. It is defined as ratio of energy stored in the cavity to the energy dissipated per cycle. It is used to measure how quickly the energy from the EM field is dissipated by the cavity.

The higher the quality factor, the slower the oscillations are damped. The analytical definition is[20]

$$Q = \omega \frac{W}{P_d} \tag{2.89}$$

W is the total energy stored in the cavity and is defined as

$$W = \frac{\varepsilon}{2} \iiint_V |E|^2 \, dV \tag{2.90}$$

It is calculated by substituting the electric field equations for the TM_{011}^{z}, Equations (2.82) through (2.84), into Equation (2.90). After performing the necessary integration and using various Bessel function properties, the total energy stored in the cavity is

$$W = \frac{\pi \varepsilon h a^2}{4} \left(\frac{B_{011}}{\omega \mu \varepsilon} \right)^2 \left(\frac{\chi_{01}}{a} \right)^2 J_1^2(\chi_{01}) \left[\left(\frac{\pi}{h} \right)^2 + \left(\frac{\chi_{01}}{a} \right)^2 \right] \tag{2.91}$$

Again, using the assumptions presented at the beginning of this section, the total power is assumed to be dissipated on the conducting walls of the cavity. The analytical representation of the dissipated power is

$$P_d = \frac{R_s}{2} \oiint_A |H|^2 \, d\bar{S} \tag{2.92}$$

where R_s is the surface resistance and is defined as

$$R_s = \sqrt{\frac{\omega \mu}{2\sigma}} \tag{2.93}$$

The power dissipated by the cavity is calculated by substituting the magnetic field equations for the TM^{z}_{011} mode, Equations (2.85) through (2.87), into Equation (2.92). After performing the necessary integration and using various Bessel function properties, the result is

$$P_d = \frac{\pi}{2}\sqrt{\frac{\omega\mu}{2\sigma}}\left(\frac{B_{011}}{\mu}\right)^2\left(\frac{\chi_{01}}{a}\right)^2 J_1^2(\chi_{01})\left[h^2 + 2a^2\right] \tag{2.94}$$

Using Equations (2.91) and (2.94) in Equation (2.89) and substituting in the resonance frequency, Equation (2.88), the quality factor for the TM^{z}_{011} resonance mode is computed,

$$Q = \frac{ha^2}{ha + 2a^2}\left(\frac{\sigma}{2}\right)^{1/2}\left(\frac{\mu}{\varepsilon}\right)^{1/4}\left[\left(\frac{\pi}{h}\right)^2 + \left(\frac{\chi_{01}}{a}\right)^2\right]^{1/4} \tag{2.95}$$

Using a permeability value of 1.257×10^{-6} H/m, permittivity value of 8.854×10^{-12} F/m, and an aluminum conductivity of 37.8×10^{6} 1/mΩ, as well as height and radius values associated with the 8-GHz MET, a typical value of Q is approximately 10400. It should be noted that during the actual operation of the MET, power is not only being dissipated by the walls, as is assumed in this derivation, but also by the plasma and cold propellant flowing throughout the chamber.

2.3 Plasma Physics

The MET transmits the microwave energy to the propellant by inducing a plasma discharge, which in turn transfers heat to the surrounding propellant. Plasma is a certain type of ionized gas that is defined as a quasineutral gas of charged and neutral particles that displays a collective behavior. It is characterized as quasineutral because it is neutral enough that the amount of electrons are assumed to be equal to the amount of ions in a specified space, but not neutral enough that certain electromagnetic forces disappear. The definition of the plasma also indicates that this collection of charged and neutral

particles display a collective behavior. This alludes to the fact that as the different particles in a plasma move, localized concentrations of positive and negative charges are generated, thereby inducing electric and magnetic fields. The magnitude of the effects of these collective fields, and therefore the plasma, on other objects are so powerful that any effects by local conditions are negligible.[21] The method by which the plasma is formed in the MET is discussed below.

2.3.1 Microwave Field Gas Breakdown

A neutral gas is transformed into plasma by way of electric breakdown. Generally, electric breakdown occurs when a sufficiently strong field is applied to a neutral material. A discharge may be ignited if the field is applied long enough and is sustained as long as the field is still present. The mechanism behind the electric breakdown of a gas is called electron avalanche. The process begins when the applied electric field increases the energy of free electrons present in the gas so that its energy exceeds the molecules' ionization potential. These highly energetic electrons proceed to collide with and ionize the neutral gas molecules, freeing an additional electron. The electric field subsequently reenergizes the two electrons to ionization energy levels. These two electrons ionize two more neutral gas molecules, each of which release another electron. This process continues in ionizing neutral gas molecules exponentially if uninterrupted. However, there are multiple mechanisms by which this electric breakdown is slowed and possibly ended.[22]

Slowing of the electron avalanche can occur when the energy transferred to the neutral molecule is not completely used for the release of an electron. The energy may be divided among different energy states, such as rotational and vibrational, within the neutral molecule, not leaving enough for ionization. Another mechanism for the slowing or overall termination of the electron avalanche can occur when free electrons diffuse away from the field or are lost to the walls of the container. The removal of these electrons decreases the probability that new electron avalanche chains will form. A third process by which electron avalanche chains are halted is recombination. In low density gases, this process is not much of a concern early on because of the low probability of an

electron encountering an ion. However, as the breakdown continues, recombination becomes a more prominent loss mechanism because of the increase in ions.

As stated before, a sufficiently strong electric field is required to cause electric breakdown and, if sustained, can support a discharge. The strength of this electric field must be strong enough to create electrons and electron avalanches faster than the loss mechanisms slowing the process down. Even if the creation rate is slightly higher than the loss rate, electric breakdown will occur and a discharge will be sustained. This field strength is known as the threshold electric field strength, E_t. For a fixed frequency and cavity geometry, the threshold electric field strength varies depending on gas pressure. This is because different loss mechanisms dominate for different pressures. The threshold electric field strengths for different gases at various pressures can be seen in Figure 2.4.

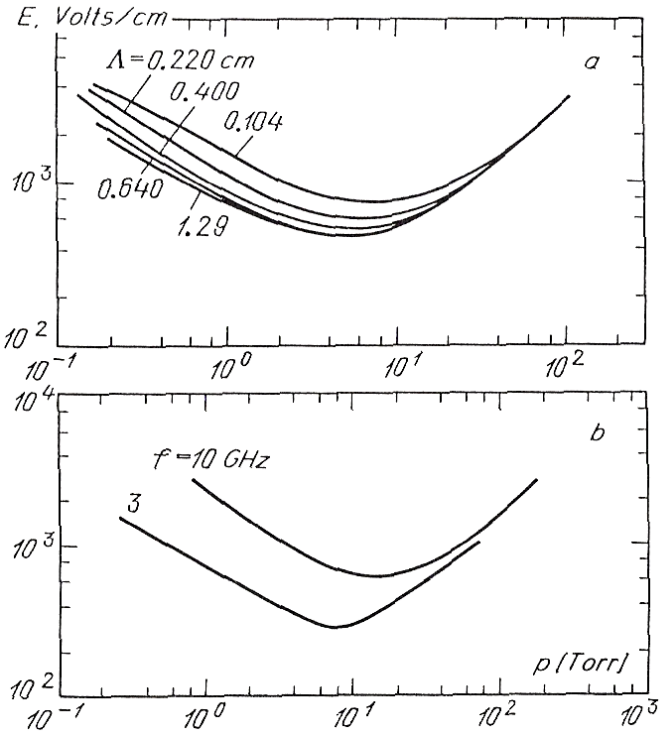

Figure 2.4 **Measured thresholds of microwave breakdown (a) air, *f*=9.4 GHz, diffusion length Λ is indicated for each curve; (b) Heg gas (He with an admixture of Hg vapor), Λ=0.6 cm. [ref. 22]**

Electron diffusion is the dominant loss mechanism for low pressure systems. This is because the distance required to be traveled by the electron to collide with a neutral is large, allowing for a greater chance in the electron traveling outside of the ionization range of the applied field. This distance is represented by the characteristic diffusion length, Λ, and is presented for a cylindrical cavity as

$$\frac{1}{\Lambda^2} = \left(\frac{\chi_{01}}{a}\right)^2 + \left(\frac{\pi}{h}\right)^2 \tag{2.96}$$

The corresponding threshold electric field strength is

$$E_t \propto \frac{\omega}{p\Lambda} \tag{2.97}$$

Note that as the characteristic diffusion length decreases, the threshold electric field strength must be increased. This means that an electron does not need to travel as far to escape the reach of the field. Subsequently the field must be increased to retain the electron for ionization.

The dominant loss mechanisms for high pressure systems are energy losses. The increase in the number of particles means that more energy is lost to excitations of other molecular energy levels (vibrational, rotational, etc.) and more collisions at insufficient ionization energy levels. The corresponding threshold electric field strength is

$$E_t \propto p \tag{2.98}$$

It should be noted that there is an optimal pressure at which the threshold electric field strength is at a minimum. This can be seen in Figure 2.4. In this region the loss mechanisms are relatively small and allow for an easier ignition and sustenance of a discharge. According to Raizer, this optimal electric break down pressure for a microwave field (convenient for the MET's operating range) has been experimentally determined to be in the range of about 1–10 torr.[22]

2.4 Propellant Chemistry

Although the MET is not a chemical propulsion system, certain chemical reactions still occur and must be taken into account with regards to energy transfer. Dissociation is one of the most influential of these chemical reactions because it absorbs energy that otherwise could be imparted to the propellant gas to increase its translational kinetic energy. Because dissociation is an equilibrium reaction, a general definition of an equilibrium reaction must be derived.

2.4.1 Equilibrium Derivation

The derivation begins with the understanding that equilibrium conditions imply that temperature and pressure do not change. This also means that the Gibbs free energy,

$$g_j = h_j - Ts_j \tag{2.99}$$

does not change.[23] This condition leads to the equilibrium criterion for J number of chemical species,

$$d\left(\sum_{j=1}^{J} N_j g_j\right) = \sum_{j=1}^{J} g_j dN_j = 0 \tag{2.100}$$

The term $dN_j = a_j d\varepsilon$, where ε represents the progress of the reaction. For a generic chemical reaction

$$a\,\mathrm{A} + b\,\mathrm{B} \leftrightarrow c\,\mathrm{C} + d\,\mathrm{D} \tag{2.101}$$

$dN_j = a_j d\varepsilon$ is expanded to

$$d\left(N_\mathrm{A}\right) = -a d\varepsilon \tag{2.102}$$

$$d(N_B) = -bd\varepsilon \tag{2.103}$$

$$d(N_C) = cd\varepsilon \tag{2.104}$$

$$d(N_D) = dd\varepsilon \tag{2.105}$$

Substituting Equations (2.102) through (2.105) into Equation (2.100), the equilibrium criterion for the generic chemical reaction becomes

$$ag_A + bg_B - cg_C - dg_D = 0 \tag{2.106}$$

Using thermodynamic relations for entropy and enthalpy, the Gibbs free energy equation can be rewritten in terms of a standard state free energy reference value, g^0_j, partial pressures of each chemical species, the total pressure of the chemical reaction, and a reference pressure. This is new Gibbs free energy equation is expressed as

$$g_j = g_j^0 + \bar{R}T\ln\left(\frac{p_j}{p}\right) + \bar{R}T\ln\left(\frac{p}{p_0}\right) \tag{2.107}$$

A combination of Equations (2.106) and (2.107) divided by $\bar{R}T$ yields

$$\frac{ag_A^0 + bg_B^0 - cg_C^0 - dg_D^0}{\bar{R}T} = \ln\left(\frac{p_C^c p_D^d}{p_A^a p_B^b}\right) + \ln\left(p^0\right)^{a+b-c-d} \tag{2.108}$$

If the left side of this equation is defined as $\ln K_p$, where K_p is the equilibrium constant and each partial pressure is converted to the species' mole fraction, X_j, then the equation for determining a generic chemical reaction's equilibrium constant is created,

$$K_p = \frac{X_C^c X_D^d}{X_A^a X_B^b}\left(\frac{p}{p^0}\right)^{c+d-a-b} \tag{2.109}$$

This equation is essential in determining the equilibrium concentrations of each species for a given temperature and pressure.[23]

2.4.2 Specific Propellant Gas Analysis

The MET has the capability of operating with a number of different propellant gases. The selection of these propellant gases is determined with the overall goal of thruster performance optimization in mind. However, other factors, such as storability and safety, can also influence which propellant gas is selected. In the past, helium and nitrogen were used for preliminary proof of concept and thruster evaluation tests. Recently, better performing and more realistic gases such as ammonia and hydrazine have been explored more thoroughly for use with the MET. The propellants used in the tests described in this thesis are nitrogen, ammonia, and simulated hydrazine and decomposition products.

Nitrogen was the first type of propellant used for this set of testing. Its dissociation equation is

$$N_2 \rightarrow 2N \tag{2.110}$$

Using a mass balance equation and the equilibrium constant equation specific to nitrogen, it can be seen that nitrogen only dissociates at very high temperatures. This fact, along with nitrogen's high molecular weight, result in poor thruster performance and a non-ideal MET propellant. However, because it is safe to use, it is an ideal proof-of-concept propellant.

Ammonia was the second type of propellant used for this set of testing. Its dissociation equation is

$$2NH_3 \rightarrow N_2 + 3H_2 \tag{2.111}$$

Because the products of this reaction include nitrogen (Equation 2.110) and hydrogen molecules, the dissociation reaction of a hydrogen molecule is

$$H_2 \rightarrow 2H \tag{2.112}$$

Mass balance equations for ammonia along with the equilibrium constant equations specific to ammonia, nitrogen, and hydrogen are used to determine the various species concentrations at different temperatures. The ammonia dissociates at relatively low temperatures, leaving only hydrogen and nitrogen molecules. Ammonia's low molecular weight makes it a propellant worth exploring for MET optimization.

Simulated hydrazine decomposition products were the final type of propellant used for this set of testing. Hydrazine itself is not used because of its many harmful properties. Instead, hydrazine is simulated by combining proportional amounts of its decomposition components. Hydrazine is different than ammonia and nitrogen in that its decomposition involves two reactions,[24]

$$3N_2H_4 \rightarrow 4NH_3 + N_2 \tag{2.113}$$

$$4NH_3 \rightarrow 2N_2 + 6H_2 \tag{2.114}$$

The first reaction is the decomposition of hydrazine into ammonia and nitrogen. The second reaction is the dissociation of ammonia into nitrogen and hydrogen (same as Equation (2.111)). Because the products of hydrazine decomposition are ammonia, nitrogen, and hydrogen, the equilibrium concentrations of each species at a given temperature and pressure are similar to that of dissociating ammonia.

The hydrazine decomposition reactions shown above can be combined into one equation, allowing for a variation in the amount of dissociated ammonia. This equation is expressed as

$$3N_2H_4 \rightarrow 4(1-X)NH_3 + (2X+1)N_2 + 6XH_2 \quad (2.115)$$

where X is the degree of ammonia dissociation with $X = 1$ being complete dissociation and $X = 0$ being no ammonia dissociation. The delivery of hydrazine to an operational MET aboard a spacecraft will pass through one of two systems that fractionally decomposed hydrazine, leaving more MET energy available for increasing the propellants' kinetic energy. These two systems are a catalyst bed followed by a plenum. The catalyst bed alone decomposes the hydrazine to about 50% dissociated ammonia. The addition of a plenum decomposes the hydrazine to about 80% dissociated ammonia. The final products of both of these pre-heating devices can be simulated in the laboratory using the proportions of each product presented below. The resulting hydrazine decomposition product proportions for a catalyst bed as well as a catalyst bed with the addition of a plenum are, respectively,

$$3N_2H_4 \rightarrow 2NH_3 + 2N_2 + 3H_2 \quad (2.116)$$

$$15N_2H_4 \rightarrow 4NH_3 + 13N_2 + 24H_2 \quad (2.117)$$

CHAPTER 3

Experimental Setup and Test Procedures

Testing of the 8-GHz MET is conducted in a laboratory located in the Propulsion Engineering Research Center at The Pennsylvania State University. The MET and its supporting components have been fabricated, collected, and assembled from many various sources spanning many years. The testing procedures presented below have been developed and used by the many different MET researchers who conducted similar experiments in the past.

3.1 Experimental Setup

The 8-GHz MET experiment consists of a variety of different components including the propellant control system and its measurement devices; the electromagnetic control system and its measurement devices; and the MET system itself. Each subsystem is discussed separately following Figure 3.1, which shows the overall arrangement of the experiment. It should be noted that chamber pressure, vacuum pressure, forward and reflected power, and strain readings are all acquired through LabVIEW data acquisition software. BNC coaxial cables are used to transmit voltage readings from the measurement instruments to a Sony Vaio PC running LabVIEW. Microwave frequency and mass flow rates are manually entered into the LabVIEW interface. All of the recorded and inserted values are saved in a spreadsheet for convenient data reduction.

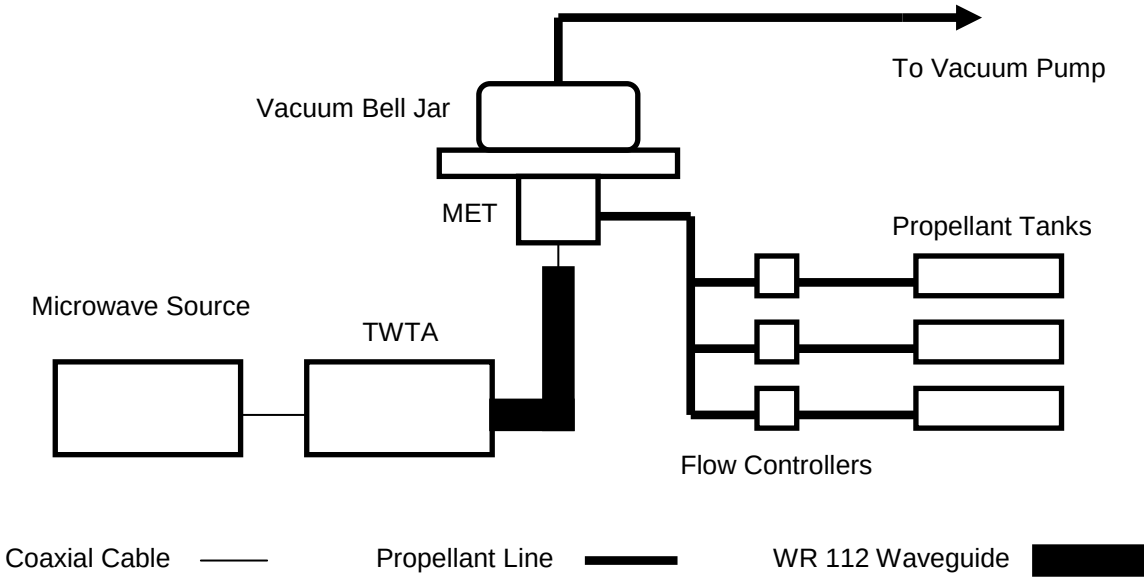

Figure 3.1 Overall arrangement of the MET experiment.

3.1.1 MET System

The MET is constructed from a block of 6061 aluminum alloy. A circular hole is bored through its center, creating a cylindrical resonance cavity. The dimensions of the cavity were determined by Clemens[18] using the resonance field equations derived in Chapter 2 for the TM^{z}_{011} resonance mode. A quartz window, sealed with an O-ring, is present towards the top of the chamber allowing for viewing of the plasma in the chamber. Two holes are drilled on opposite sides of the chamber, extending tangentially from the circular cavity. This induces the plasma-stabilizing propellant swirl. These holes are created such that a variety of different sized injectors can be interchanged and parametrically tested in the MET. A third hole is drilled perpendicular to the circular cavity allowing for chamber pressure measurements. Four holes located at the corners of the chamber are drilled, allowing for the assembly of the base and nozzle plates with the chamber, as well as attaching the entire assembly to the vacuum flange plate. O-ring grooves are formed at the top and bottom of the chamber in order to vacuum seal the contact surfaces of the chamber with the nozzle and base plates respectively. There are two versions of the MET currently in existence at Penn State, as described in Chapter 1.

The only difference being that one chamber has a separation plate positioned on its axial center, separating the antenna from the low pressure plasma. It is vacuum sealed at its contact surfaces using two O-rings. All other components of these chambers are identical.

The base plate of the MET is also made of 6061 aluminum alloy and is sized to match the length and width of the chamber. A small hole is drilled through its center to allow for the insertion of the antenna. The height of the base plate is sized such that the antenna is inserted into the cavity at the optimal electromagnetic resonance depth. An O-ring groove and four small threaded screw holes are drilled into the bottom of the base plate, allowing for the attachment and vacuum sealing of the N-type coaxial panel mount connector which contains the antenna probe.

Many different nozzle plates were parametrically tested to assess the performance variation among them, with a goal of finding the best performing configuration. Six stainless steal converging only nozzle plates and one tungsten converging–diverging nozzle plate, all with different throat diameters, were used in testing.

3.1.2 Propellant Control System

The propellant control system includes all aspects of the experimental setup pertaining to the control and measurement of the propellant gases through the MET experiment. The different propellants are compressed and held in storage tanks until they are needed for experimentation. The gases are controlled using a number of different sized gas specific flow controllers and transported through a single feed line to the MET. The line is then split and the propellant enters the chamber tangentially on opposite sides of the cavity. The heated propellant is subsequently exhausted through the nozzle, into a vacuum bell jar. A vacuum pump is connected to the bell jar through the same flange plate at which the MET is attached. The exhaust gas is pulled out of the bell jar and exhausted through the laboratory's ventilation system. The propellant flow rates are measured through a multi-gas flow controller and the chamber and vacuum pressures are measured using a pressure transducer and capacitance manometer respectively. Figure 3.2 shows a schematic of this system, followed by a list of the various components.

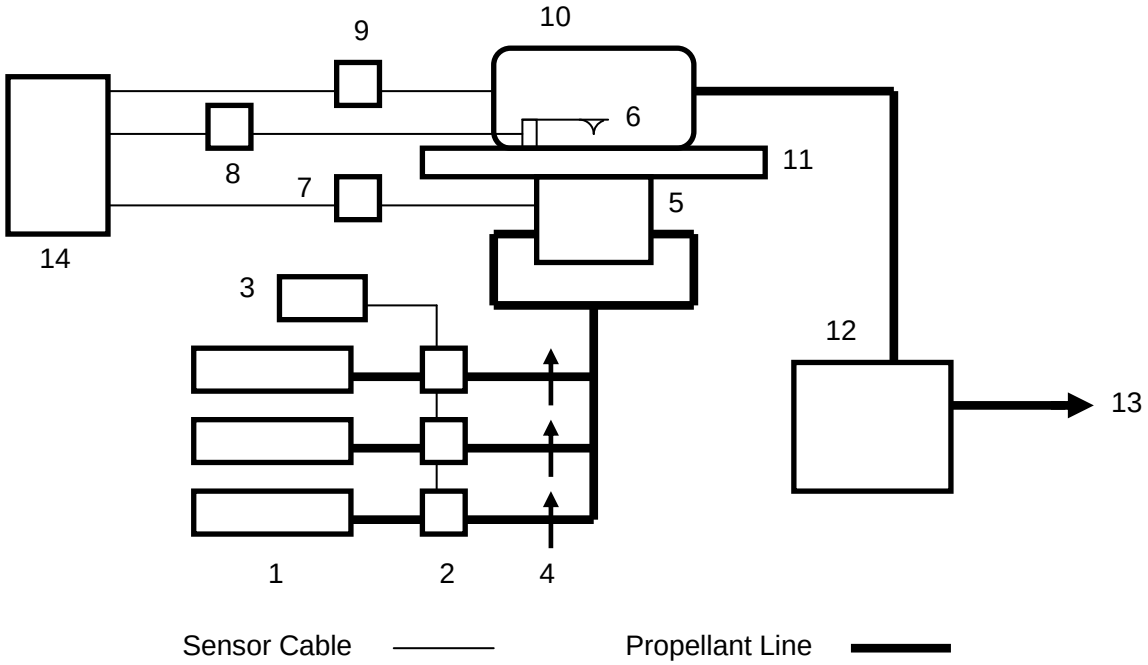

Figure 3.2 MET propellant control system.

1) Propellant Tanks (NH_3, H_2, N_2)
2) Unit Mass Flow Controllers
   a) UTS-8100 5 SLM N_2
   b) UFC-1660 10 SLM N_2
   c) UFC-8100 1 SLM NH_3
   d) UFC-1660 2 SLM NH_3
   e) UFC-1100A 500 SCCM N_2
3) MKS Multigas Controller 147
4) Propellant Line Ball Valves
5) MET
6) Thrust Stand
7) Omega Pressure Transducer Sensor and Meter

8) Thrust Stand Meter
   a) Instruments Division Wide Range Strain Indicator
   b) Philtec 12V Optical Sensor
9) Hastings Instruments HCM-300 Capacitance Manometer Sensor and Meter
10) Vacuum Bell Jar
11) Vacuum Flange Plate
12) Welch 1402 DuoSeal Vacuum Pump
13) To laboratory ventilation system
14) Chamber pressure, vacuum pressure, and deflection measurement acquisition using LabVIEW installed on Sony Vaio PC

Depending on the objective of the test being conducted, a thrust stand is inserted in the bell jar above the nozzle plate, with the intent of measuring the thrust of the MET by using the exhausted propellant's momentum. The thrust stand used in this experimentation is the same one operated by Clemens[16] and is based off of Welander's[14] thrust stand design. It uses a flexible beam that is clamped at one end and has a momentum trap hanging from the other. Theoretically, the exhaust gas' momentum is caught in the momentum trap and subsequently results in the deflection of the beam. Strain gauges mounted on the beam measure the deflection which is converted into a force measurement using a known deflection-to-weight correspondence attained through prior calibration. However, because this system did not provide accurate results, which will be discussed in following sections, a new deflection cone based on Clemens[18] 2.45-GHz MET thrust stand was fabricated. The concept behind the deflection cone is the same as that of the momentum trap. Again, this system proved to be inaccurate, and it was decided to forgo the strain gauge system and implement an optical measurement system. This system also used the clamped flexible beam with the deflection cone design and subsequent momentum capture theory, but instead used a distance measuring optical device to measure the deflection of the beam. This system also failed to provide accurate measurements and focus was then turned towards thruster optimization. Schematics of the three different thrust measurement designs are shown in Figure 3.3.

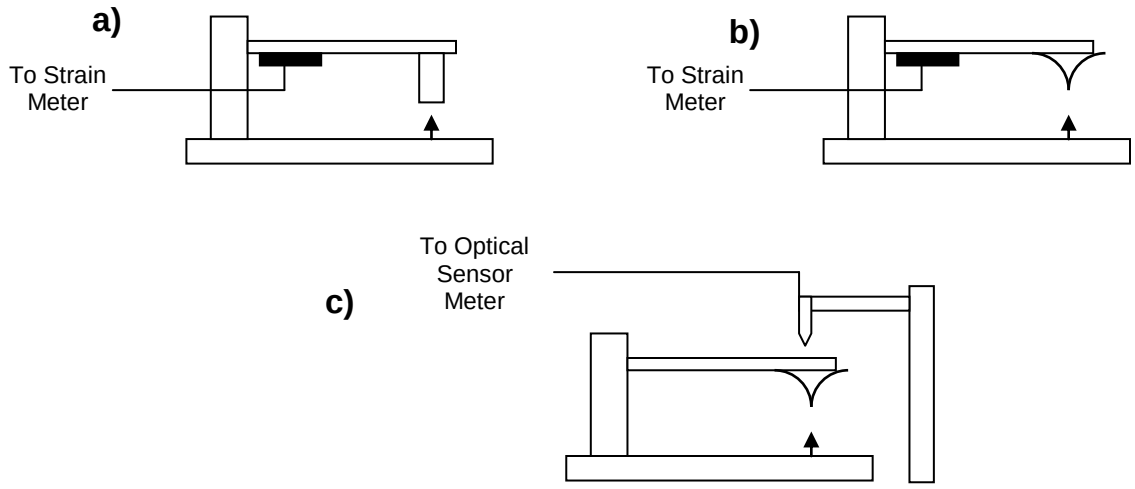

Figure 3.3 **MET thrust stand arrangements. (a) thrust stand with momentum trap and strain gauge; (b) thrust stand with deflection cone and strain gauge; (c) thrust stand with deflection cone and optical sensor.**

3.1.3 Electromagnetic Control System

The electromagnetic control system includes all aspects of the experimental setup pertaining to the control and measurement of the 8-GHz microwave signal through the MET experiment. The signal is created using a HP 8684B 5.4-GHz to 12.5-GHz range signal generator and is transferred to an MCL MT3200A traveling wave tube amplifier (TWTA) through an N-type coaxial cable. The TWTA amplifies the signal to the desired power level and transmits it to a series of attached WR112 waveguide sections. The waveguide system is designed to deter a reflected signal from entering the TWTA in order to avoid damage. After traveling through a series of straight and bent waveguide sections, the signal enters a three-port circulator, which acts as a one way path for the microwave signal. The microwaves enter the circulator through the first port and exit through the second port into a bidirectional waveguide coupler. This section of waveguide has two power connectors attached to its sides, allowing for forward and reflected power measurements using HP and Agilent power sensors. The microwave signal is transitioned from waveguide transmission back to coaxial transmission through a waveguide to coaxial transition piece. The signal is finally transmitted into the MET resonant cavity through an N-type panel mount connector with an antenna probe extending into the cavity. TM^{z}_{011} resonance mode fields are produced in the MET cavity

and avalanche ionization of the injected propellants begins, creating a coalesced plasma. Any waves reflected back from the chamber due to mismatch travel through the bidirectional coupler and are directed into the second port of the three-port circulator. The reflected signal is subsequently directed out of the third port and into a dummy load. These reflected signals are converted into heat and convected away from the dummy load by cooling fans set up around the experiment. Figure 3.4 shows a schematic of this system, followed by a list of the various components.

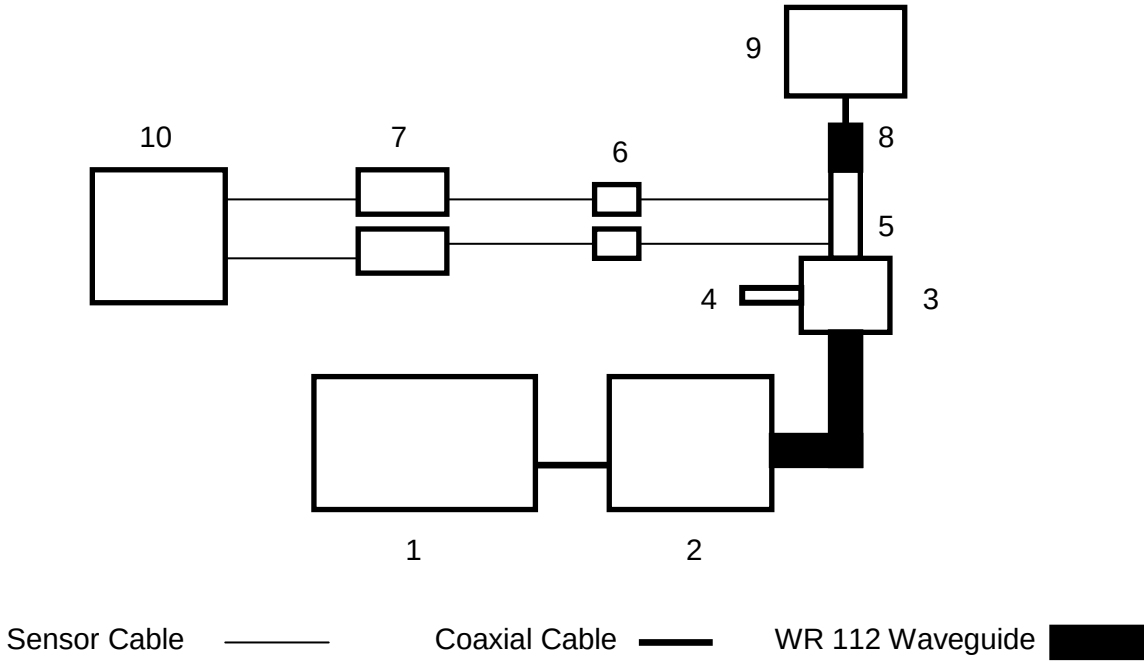

Figure 3.4 MET Electromagnetic control system.

1) HP 8684B 5.4–12.5-GHz Signal Generator
2) MCL MT3200A TWTA, 7.9–8.4-GHz Freq Range, 350 W Max Power
3) Channel Microwave Corp. Three Port Circulator (WR112)
4) ATM WR112 Reflected Signal Dummy Load
5) ATM WR112 Bidirectional Coupler
6) HP and Agilent Power Sensors
7) HP 437B Power Meters
8) WR112 to N-type Coaxial Transition
9) MET
10) Power measurement acquisition using LabVIEW installed on Sony Vaio PC

3.2 Testing Procedures

Once the experiment is set up and all of the instruments are turned on, MET performance evaluation and optimization can be conducted. Several steps must be taken in order to perform an accurate and useful test. These steps may vary depending on the objective of the tests being performed, but most tests are fairly similar and are generalized in the following sections. There are three primary testing procedures performed in gathering performance data. The first procedure is the thrust stand calibration in which data is collected to convert beam deflections to thrust measurements. The second procedure is the cold flow process. Cold flow values are useful in the evaluation of the MET's performance in a number of ways. The first set of important information useful in performance evaluation is that the cold flow values are easily measured and can verify the thrust measurements made by the thrust stand using performance equations discussed in Chapter 2. The cold flow values are also essential in determining the relationship between the Reynold's number and the discharge coefficient. Finally, they aid in calculating the performance of the MET while in operation. Chamber temperatures are not measured during hot fire operation and must be calculated. The pressure values obtained during cold flow and hot fire operation at a given mass flow rate are substituted into their respective mass flow equation in order to obtain a hot and cold temperature ratio. Known pressure and temperature dependant chemical equilibrium constants obtained from sources such as the NASA Lewis chemical equilibrium program are solved simultaneously with the temperature ratio equation to produce a hot fire chamber temperature, and ultimately characterize the performance of the MET. The third and final testing procedure is the process by which hot fire data is collected.

3.2.1 Thrust Stand Calibration

All of the thrust stand configurations described above are calibrated in the same manner. The momentum trap or deflection cone is attached to one end of the beam and centered over the nozzle exit hole, while the other end of the beam is clamped. Known

weights ranging from 1 mg to 2 g are incrementally placed directly over the center of the momentum trap or deflection cone with the corresponding voltage changes being recorded. In order to avoid hysteresis effects, the zero weight voltage reading is recorded in between each weight placement. This procedure is repeated multiple times to avoid any isolated anomalies and a linear relationship between the amount of weight placed on the beam and the measured voltage change (i.e., strain on the beam) is created. This curve can now be used to convert recorded voltage changes during cold and hot fire operation to useful thrust measurements.

3.2.2 Cold Flow Procedure

Before the cold flow procedure can commence, the MET chamber and the bell jar must be evacuated by activating the vacuum pump. The pressure transducer consistently indicated that a vacuum was achieved in the MET chamber, implying an absence of leaks. The lowest vacuum pressure in the bell jar achieved as measured by the capacitance manometer was approximately 0.250 torr. Once a vacuum is achieved, the desired propellant gas tanks are opened and pressurized. The desired flow rates, controlled by the mass flow controller(s), enter the chamber at fixed increments. When the chamber pressure and vacuum pressure equalize at a given flow rate, the pressure values, along with the thrust stand deflection measures (if applicable) are recorded by a LabVIEW software application. The incremental value between flow rates is determined by the nozzle's throat diameter and is intended to capture an accurate representation of the thruster's performance at an appropriate resolution. Smaller nozzle throat diameters require smaller increments due to the greater magnitude of the difference in chamber pressures between flow rates. The maximum flow rate reached during cold flow testing is estimated by reviewing the maximum flow rates attained by previous hot fire tests with nozzles of similar throat diameters. It should be noted that during cold flow tests involving the thrust stand, the flow rates are returned to the zero point between each flow increase to avoid any significant hysteresis effects on the flexure. This procedural change took affect after a series of inaccurate data resulting from not returning the flow rate to zero after each flow value was recorded.

3.2.3 Hot Fire Procedure

MET operational testing, also known as hot fire testing, is always conducted directly following a cold flow test. This ensures the least amount of variation between environmental conditions which can alter the results of the tests. Once the signal generator and TWTA are activated, the chamber is evacuated to a pressure in which electrical breakdown can be initiated. This pressure can be less than or equal to approximately 0.50 psia. The input power is subsequently increased to approximately 100 W, igniting a diffuse plasma in the chamber. The propellant flow rate and input power are simultaneously increased to the desired respective starting values. Once these values are achieved, the TWTA is commanded to hold the input power level constant and hot fire data recording can begin. The flow rate values and fixed increment value used for each hot fire test are the same values used for the preceding cold flow test. This allows for the simplest method of pressure ratio calculation. The microwave signal frequency is adjusted at each flow rate in order to obtain the highest coupling efficiency (P_{abs}/P_{for}) possible. The chamber and vacuum pressures are allowed to equilibrate and are subsequently recorded along with the various power readings and thrust stand deflection measures (if applicable) using LabVIEW. Hot fire testing is completed when the flow controller reaches its maximum flow rate, the performance of the thruster has been visibly declining for a significant amount of preceding flow rates, or the plasma is extinguished.

CHAPTER 4
Experimental Results

The tests conducted on the MET serve two purposes. The first purpose is to obtain accurate thrust measurements through the use of a reliable thrust stand. The second purpose is to optimize the performance of the MET by parametrically testing a number of different thruster parameters, including antenna depth, injector diameter, nozzle material and throat diameter, and propellant gas. The results of these tests are presented in the sections below.

4.1 Cold Flow Nitrogen Thrust Stand Results

Although theoretical performance calculations are essential in producing the highest performing thruster, thrust measurements are used as a direct measure of MET performance. Theoretical values, such as various chemical equilibrium constants, actual chamber temperatures, etc., are only as accurate as the assumptions and approximations used to calculate them. Thrust measurement is a real-time measure of thruster performance and can help either to reinforce or to disprove the accuracies of the theoretical calculations.

There were a number of different configurations used to obtain thrust measurements; however, all used the same calibration technique described in Chapter 3. Figure 4.1 is an example of a thrust stand calibration chart where measured strain values are converted to thrust values.

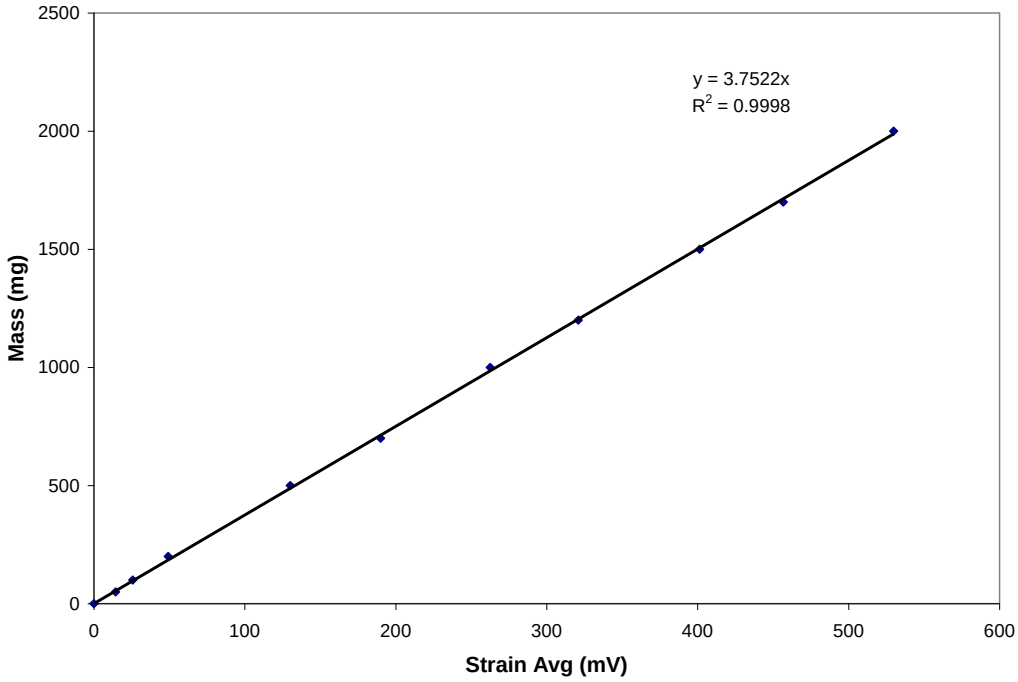

Figure 4.1 Thrust stand calibration curve with equation for linear fit.

The following sections present the results of the four different variations of thrust stand and measurement device combinations used in an attempt to collect direct thrust measurements of the MET. These variations are a momentum trap measured with a strain gauge, a deflection cone measured with a strain gauge, a deflection cone measured with an optical sensor, and an optical sensor measuring the deflection of the MET supported by a flexible waveguide. It should be noted that all of the thrust stand tests presented in this section were performed using nitrogen gas as the propellant.

4.1.1 Momentum Trap

The principle behind the momentum trap thrust stand is that the exhaust gas of the MET is collected by a cylinder positioned directly above the nozzle exit. The momentum of the gas is transferred to the momentum trap after impinging on a deflection cone positioned at the top of the trap. The momentum collected by the cylinder subsequently deflects the beam to which it is attached, creating strain in the beam that is measured by a strain gauge. As stated above, this strain is then converted into a thrust measurement

using the previously obtained calibration curve. These measured thrust values are compared to the theoretical thrust values calculated using the chamber and vacuum pressure measurements along with the performance evaluation equations found in Chapter 2. Figure 4.2 displays the comparison of momentum trap thrust measurements to the theoretical thrust values obtained from the pressure measurements.

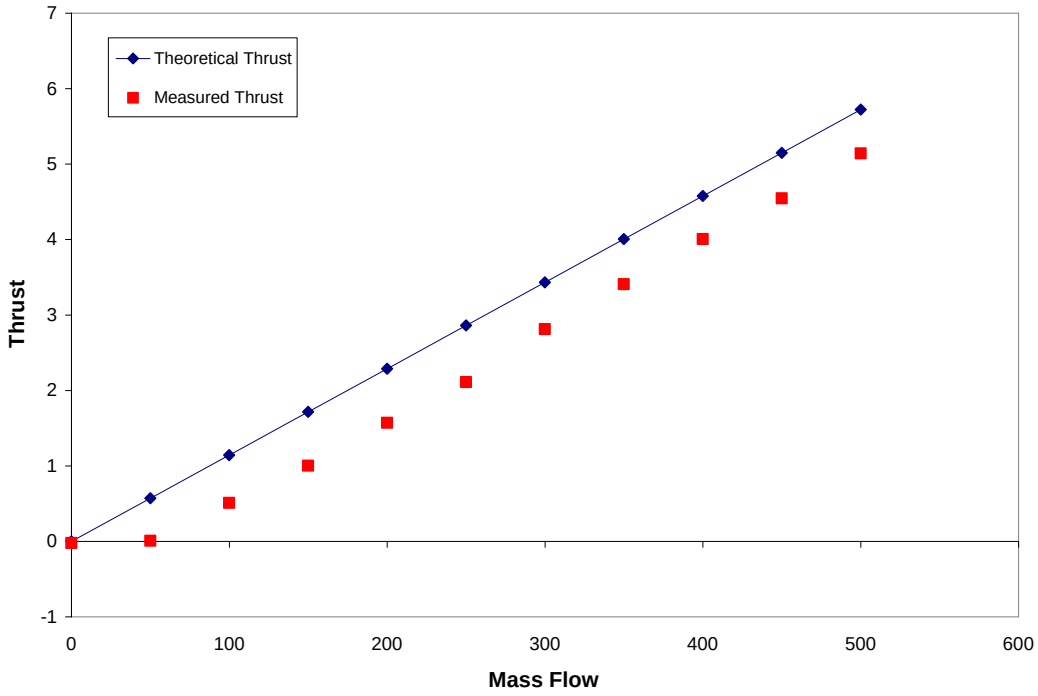

Figure 4.2 **Cold flow momentum trap comparison of measured thrust to theoretical thrust.**

The measured thrust is an average of about 0.65 mN lower than the theoretical thrust, which translates to an 11% difference when compared to the maximum theoretical thrust recorded. This is a substantial difference that needs correcting. These observations can possibly be attributed to hysteresis of the beam and strain gauge drift which were a result of the cold flow thrust measurement method. This method increased the mass flow rate after each measurement was taken. All of the strain difference values measured at the desired flow rates were based off of the original zero flow measurement. An alternate method of cold flow thrust measurement was created in an attempt to combat these effects and provide more accurate thrust values. This method returned the mass flow rate to zero after each incremental mass flow measurement where the corresponding strain

measurements were recorded. The strain difference for each mass flow was calculated using either the preceding or subsequent zero value, instead of the single beginning zero value. Both adjacent zero values produce similar results. The results of the new testing method are displayed in Figure 4.3. It should be noted that all cold flow tests presented henceforth use this alternate testing method.

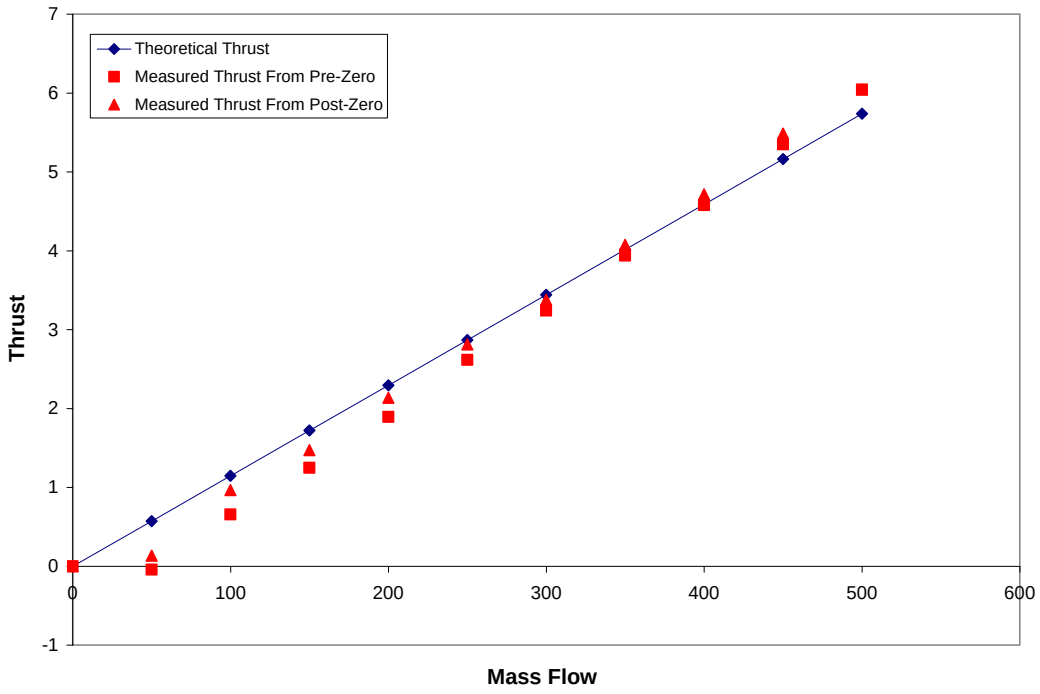

Figure 4.3 **Cold flow momentum trap comparison of measured thrust to theoretical thrust using alternate cold flow measurement method. Both pre-zero and post-zero based strain measurements are displayed.**

The new cold flow testing method seemed to have partially corrected the thrust stand measurements, providing more accurate thrust values. The average difference for the preceding zero strain calculation method is about 0.18 mN, which equates to a 3% difference when compared to the maximum theoretical thrust value. The average difference for the subsequent zero strain calculation method is about 0.03 mN, which equates to a 0.5% difference when compared to the maximum theoretical thrust value. However an aspect of the previous method's results still remains in the alternate testing method's results. At a mass flow of 50 sccm, a theoretical thrust should be present;

however, the measured thrust is either essentially zero or even negative. This shows that the momentum trap is unable to measure low thrust values and may require an alteration. The problem may be that either a small amount of exhaust gas is diffused and does not completely enter the momentum trap, or the momentum trap is too massive to be moved by the small amount of impinging gas. A solution to both of these problems may be to use a deflection cone instead of a momentum trap.

4.1.2 Deflection Cone

A deflection cone is essentially the top portion of the momentum trap without the surrounding cylinder. It is lighter in weight, and the tip of the cone extends closer to the nozzle than the momentum trap's cone, allowing for more immediate momentum transfer. Figure 4.4 shows a cold flow test using the deflection cone. Note that, as before, the thrust measurements using both the preceding and subsequent adjacent zero values are displayed.

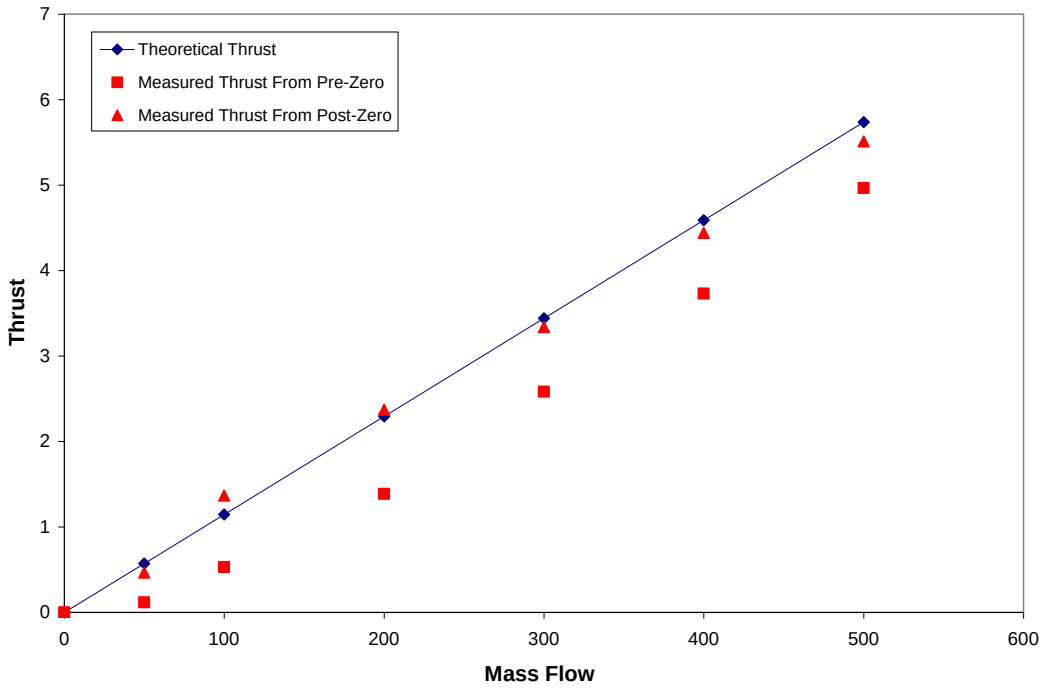

Figure 4.4 **Cold flow deflection cone comparison of measured thrust to theoretical thrust. Both pre-zero and post-zero based strain measurements are displayed.**

The results of this test show that the thrust values measured using the preceding adjacent zero values to calculate strain produce the similar inaccurate results that were found when using the momentum trap. Specifically, an average difference of 0.63-mN was found between the measured and theoretical thrust values, which corresponds to an 11% difference when compared to the maximum theoretical thrust value recorded. However, the thrust measurements from the deflection cone appear to be more accurate throughout the entire range of flows, including the 50-sccm flow rate value, when the subsequent adjacent zero values are used in calculating strain. Specifically an average of 0.04-mN difference between the measured and theoretical thrust values, which corresponds to a 0.7% difference when compared to the maximum theoretical thrust value recorded.

Although the thrust value obtained from the post-zero based strain calculations agree with the theoretical thrust, the fact that both the pre-zero and post-zero based thrust calculations do not agree is cause for concern. This means that the strain reading for the zero flow value before the desired flow rate is not equal to the strain reading for the zero flow rate after the desired flow rate. In other words, the zero point drifted. The possible cause of this problem is thermal expansion of the flexible beam cause by the propellant hitting the beam in a vacuum environment. This causes an inaccurate inflation of the strain value. The thrust calculated from this inflated strain measurement only appears to agree with the theoretical thrust measurements. Insulating the beam was attempted; however, the results were the same. Conduction from the deflection cone to the beam has a greater effect on the thermal expansion of the beam than the convection from the surrounding gas. This realization led to the introduction of a different beam deflection detection method in which a distance-measuring optical sensor positioned above the flexure replaced the strain gauge.

4.1.3 Optical Beam Deflection Detection Results

The optical sensor uses a light emitting probe that senses the distance between itself and the flexible beam. This distance is translated into a voltage and subsequently can be used to calculate thrust from a set of calibration data. The calibration data is

acquired in a similar manner as the strain gauge using known weights to observe the beam deflection. The sensor's probe was positioned directly above the center axis of the deflection cone, which is in line with the nozzle exit. Figure 4.5 displays the results of a thrust stand test using the optical sensor to measure beam deflection.

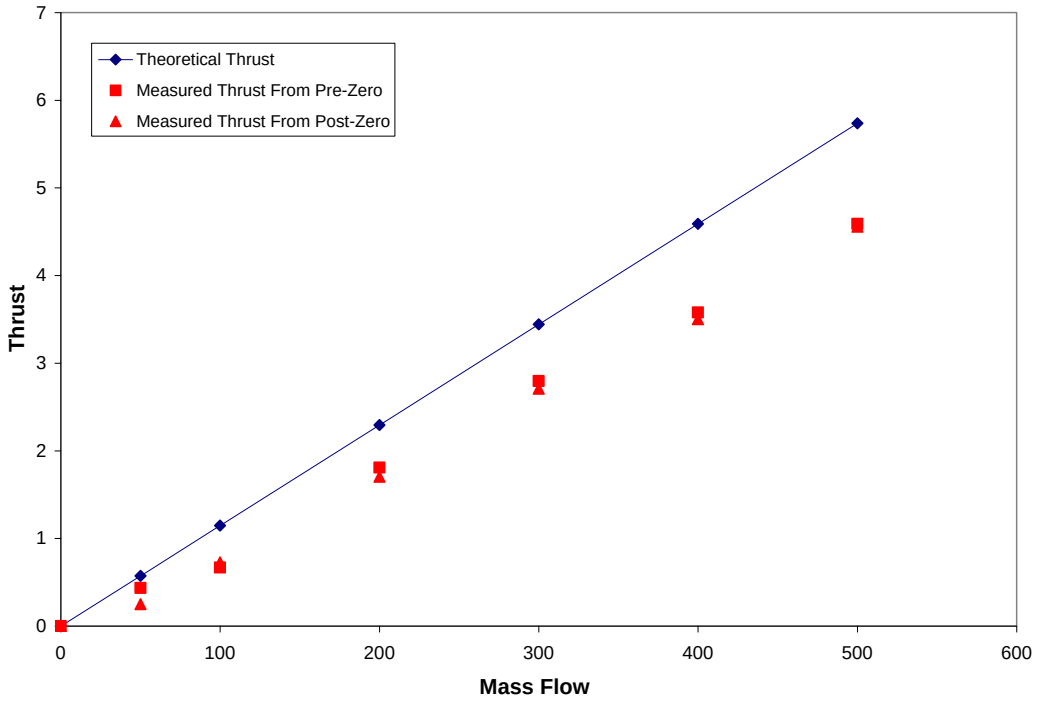

Figure 4.5 **Cold flow deflection cone comparison of measured thrust to theoretical thrust using an optical sensor to measure beam deflection. Both pre-zero and post-zero based strain measurements are displayed.**

Both the pre-zero and post-zero based strain measurements are almost equal. This indicates that the thermal expansion of the beam does not affect the beam deflection measurements obtained using the optical sensor. However, once again the measured thrust is less than the theoretically calculated thrust. Specifically for the preceding adjacent zero based strain calculation, an average of 0.65-mN difference exists between the measured and theoretical thrust values, which corresponds to an 11% difference when compared to the maximum theoretical thrust value recorded. And for the subsequent adjacent zero based strain calculation, an average of 0.72-mN difference exists between the measured and theoretical thrust values, which corresponds to a 12.5% difference when compared to the maximum theoretical thrust value recorded.

The measured thrust values obtained using the deflection cone are consistently 11% or 12% less than the theoretically predicted thrust. Perhaps not all of the exhausted gas between the nozzle and the deflection cone is impinging on the deflection cone due to diffusion, resulting in a lower measured thrust. In an attempt to test this theory, the thrust stand was lowered to half of its original height, ensuring that more of the exhaust gas reaches the deflection cone. Figure 4.6 presents the results of an experiment testing this idea.

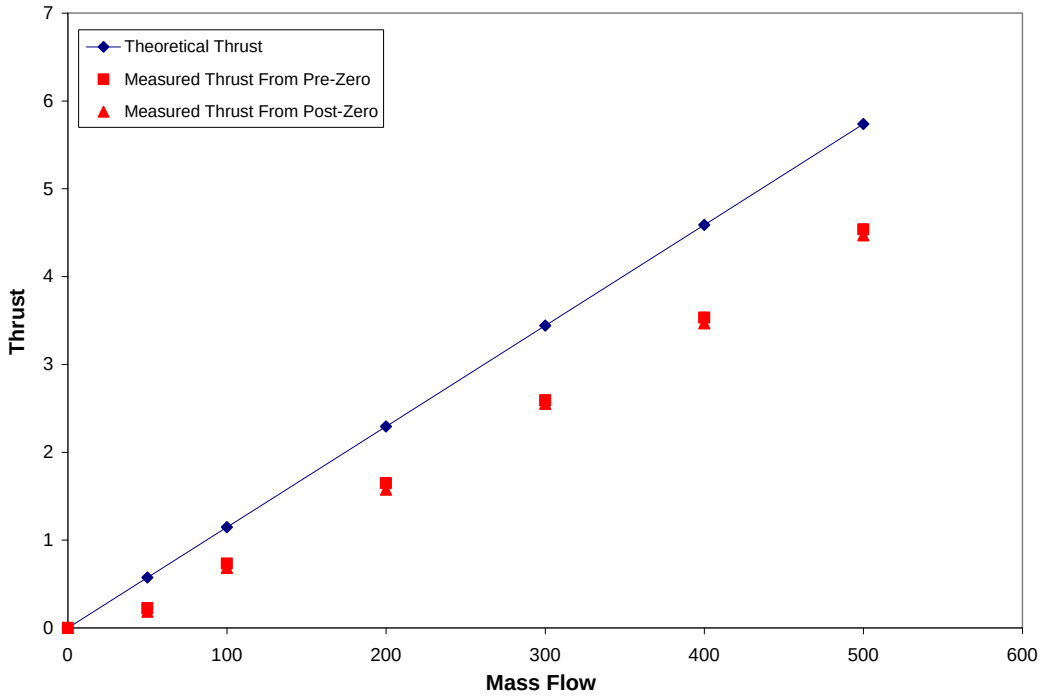

Figure 4.6 **Cold flow deflection cone comparison of measured thrust to theoretical thrust using an optical sensor to measure beam deflection at half thrust stand height. Both pre-zero and post-zero based strain measurements are displayed.**

The data show that the same problem continues to occur. In fact, lowering the thrust stand had almost no effect on the measured thrust. For the preceding adjacent zero based strain calculation, an average of 0.64-mN difference exists between the measured and theoretical thrust values, which corresponds to an 11.5% difference when compared to the maximum theoretical thrust value recorded. And for the subsequent adjacent zero based strain calculation, an average of 0.69-mN difference exists between the measured

and theoretical thrust values, which corresponds to a 12% difference when compared to the maximum theoretical thrust value recorded.

The final method of direct thrust measurement attempted was supporting the MET chamber with only a flexible waveguide and placing the optical sensor above the MET. Theoretically the thrust produced by the MET would deflect the flexible waveguide. This deflection would then be converted into thrust measurements using calibrated data acquired similarly to the previous methods. The MET required a flexible waveguide rigid enough to support its weight. However, the magnitude of the thrust produced during cold flow operation was not enough to deflect the flexible waveguide. A more flexible waveguide was acquired and the MET waveguide system was supported with springs. Again, the same issue occurred; the spring needed to be rigid enough to support the weight of the MET chamber; however the cold flow thrust could not deflect the spring enough to take thrust measurements. It was determined that it was impossible to detect a thrust deflection in a system that supports the MET chamber because the thrust values are negligible compared to the weight of the MET. Research focus was then turned towards thruster optimization.

4.2 Nitrogen Results

The MET chamber was originally designed with a dielectric separation plate located in the center of the cavity. The purpose of this separation plate was to isolate the antenna from the propellant gases that could cause the formation of a plasma at the base of the chamber. This plasma could potentially damage the antenna, rendering it useless. However, this separation plate, typically made of brittle materials such as quartz, boron nitride or a similar ceramic, has a probability of shattering during launch or shock separation events. One of the motivations of the design of this new 8-GHz MET was to create a chamber without a separation plate in order to avoid this potential problem. This chamber was fabricated from a single piece of aluminum. The antenna is insulated from any plasma located at the base of the chamber with a dielectric antenna cap made from either Teflon or fluoroloy. Preliminary hot fire testing of the 8-GHz MET without a separation plate was conducted using nitrogen and simulated hydrazine.

The nitrogen testing produced a coalesced plasma similar to that produced with the 2.45-GHz and 7.5-GHz MET chambers. Results were obtained by Clemens[18] using this thruster configuration; however, the dielectric cap would periodically ablate because of the formation of a plasma at the base of the chamber, causing damage to the antenna. The ablation of the antenna caps continued in tests performed during the timeframe of the work reported in this thesis. A picture of these ablated antenna caps and damaged antennas is displayed in Figure 4.7.

Figure 4.7 **Antennas and antenna caps: (right) new antenna and antenna cap; (left) damaged antennas and antenna caps.**

This problem prompted the decision to design a new 8-GHz MET chamber containing a dielectric separation plate. All other aspects of this new chamber are identical to the original one piece 8-GHz MET chamber. Note that a dielectric antenna cap is unnecessary because of the addition of a separation plate. Testing of the new chamber was conducted in order to compare performance results with that of the one piece chamber. Similar results correspond to similar behavior and allow for further optimization of the MET. The parameter used to compare the two chambers is the ratio of hot fire chamber pressure to cold flow chamber pressure at a given flow rate. This ratio, as described in Chapter 3, is an indication of the chamber temperature and, therefore, I_{sp} performance of the MET. These tests were conducted using nitrogen gas as the propellant. The results of this test are shown in Figure 4.8.

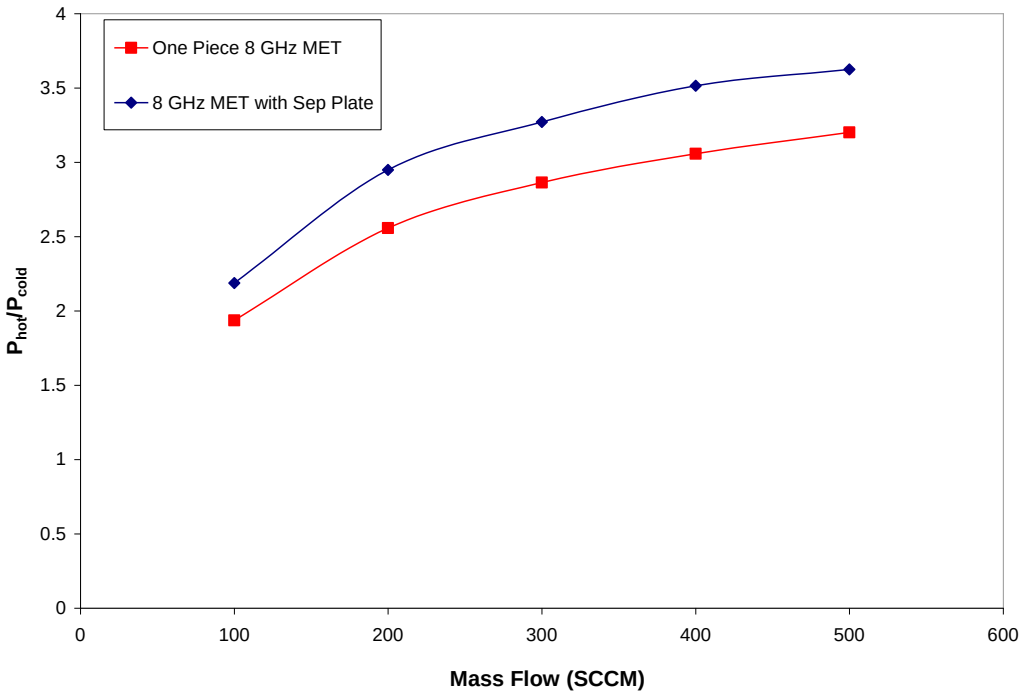

Figure 4.8 **Comparison of the one piece 8-GHz MET pressure ratio with the 8-GHz MET with a separation plate pressure ratio using nitrogen propellant.**

These results show that the chamber with the separation plate exceeds the performance of the one piece chamber without a separation plate, allowing thruster evaluation and optimization to continue. However, as discussed in Chapter 2, nitrogen is not the ideal propellant for use with the MET due to its high molecular weight. Therefore the optimization of the 8-GHz MET with a separation plate, henceforth referred to as just the 8-GHz MET, is continued using better performing propellants ammonia and simulated hydrazine.

4.3 Ammonia Results

The 8-GHz MET was parametrically optimized using ammonia gas as the propellant. Ammonia gas is an ideal propellant for the MET for various reasons. The ammonia molecule is lightweight, it dissociates at relatively low temperatures, and ammonia is liquid storable. It is also easier to test with considering the layout of the experiment in the lab. Ammonia tests require only one gas tank and mass flow controller

to operate. Simulated hydrazine tests require three separate gas tanks and mass flow controllers to operate correctly. It should be noted that in this section and the simulated hydrazine results section both chamber pressure values and specific power values ($P_{for}/\dot{m}$) are normalized to a baseline testing configuration. All of the performance evaluation values, however, are absolute.

Before flow-related parameterization can begin, the electromagnetic fields created in the cavity must be optimized to ensure maximum absorption of the microwave energy by the propellant. Field optimization is achieved by varying the shape of the antenna tip and the antenna's depth into the chamber. The antenna protrudes into the chamber at a certain baseline depth configuration. The antenna's protuberance into the chamber is reduced by the amount presented (50%, 75%, and 88%) for each subsequent antenna configuration. As with the nitrogen hot fire test, pressure ratios calculated for each antenna variation are used to determine performance. Figure 4.9 displays the antenna optimization results where two different tip shapes, rounded and flat, at various depths were considered.

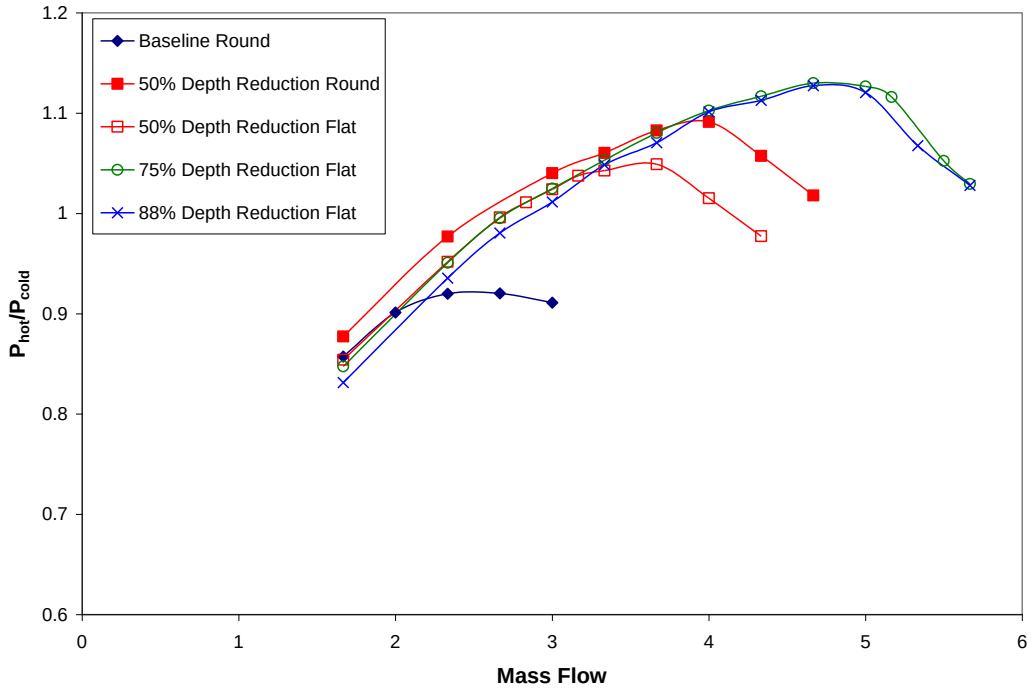

Figure 4.9 **Normalized comparison of pressure ratios for various antenna depths and shapes using ammonia propellant.**

The optimal antenna configuration is the 75% reduced depth with a flat tip. It should be noted that although the 50% reduced depth antenna with a round tip outperformed the 50% reduced depth antenna with a flat tip, the implementation of a 75% reduced depth antenna with a round tip was disadvantageous. A section of the rounded tip of this antenna would have been beneath the bottom surface of the cavity, creating variations in the generated electromagnetic field.

4.3.1 Flow Related Optimization

Flow related optimization includes the parametric performance analysis of flow control devices located on the MET. The propellant injectors and the nozzle are the two flow control components of the MET that can be parametrically optimized. The injectors control the inflow of propellant and the subsequent behavior of the propellant swirl inside the cavity. The nozzle controls the outflow of the propellant from the chamber. The performance evaluation and ultimate optimization of both flow controller components is presented below, beginning with the propellant injectors.

4.3.1a Injector Optimization

The propellant injectors' function is to regulate the influx of mass flow and swirl behavior. This is accomplished by varying the injector diameter. A smaller diameter results in a higher flow velocity for the same mass flow rate, which in turn produces a tighter plasma stabilizing propellant swirl. The optimized configuration is based on three performance values calculated using the chamber pressures, input powers, and reflected powers collected during testing. The first performance value is the coupling efficiency, which is a measure of the power absorbed by the plasma. This is calculated using the forward and reflected power measurements,

$$CE(\%) = \frac{P_{\text{for}} - P_{\text{ref}}}{P_{\text{for}}} = \frac{P_{\text{abs}}}{P_{\text{for}}} \tag{4.1}$$

The second value calculated for performance evaluation is the thermal efficiency,

$$\eta_T = \frac{\Delta C_p T_c \dot{m}}{P_{\text{for}}} \tag{4.2}$$

which is the ratio of propellant specific enthalpy to specific forward power. This value is a measure of the amount of power that is directly used to increase the chamber temperature.

The third value calculated for performance evaluation is the specific impulse, I_{sp}, of the thruster. The pressure values obtained during cold flow and hot fire operation at a given mass flow rate are substituted into their respective mass flow equation in order to obtain a hot and cold temperature ratio. Known pressure and temperature dependant chemical equilibrium constants obtained from sources such as the NASA Lewis chemical equilibrium program are solved simultaneously with the temperature ratio equation to produce a hot fire chamber temperature. This chamber temperature is substituted into the performance calculation equations presented in Chapter 2 to ultimately calculate the I_{sp}. All of these performance evaluation values (coupling efficiency, thermal efficiency, and specific impulse) are plotted against the chamber pressure normalized to a baseline configuration.

The propellant injector optimization consists of two series of tests using different pairs of injectors. Each series tests the chamber conditions at three fixed power levels (150, 200, and 250 W). The diameter of the injectors in the second series of tests are double that of the injectors in the first series of tests. The effects of this variation can be seen in Figures 4.10 through 4.12.

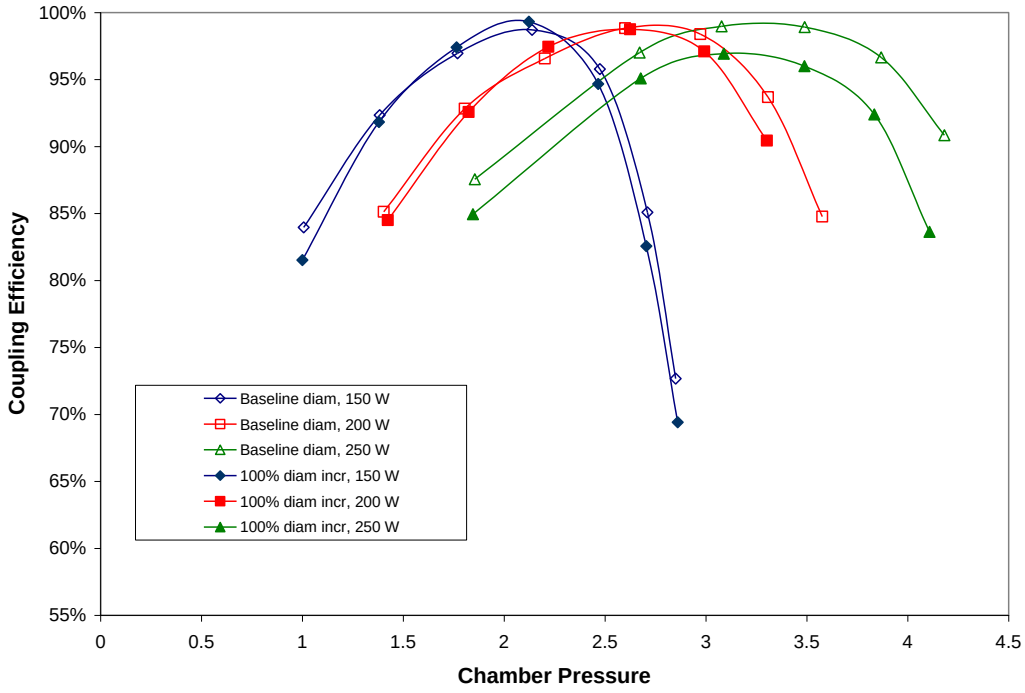

Figure 4.10 **Coupling efficiency vs. normalized chamber pressure comparison of injectors with a baseline diameter and a 100% increase of the baseline diameter at 150, 200, and 250 W using ammonia propellant.**

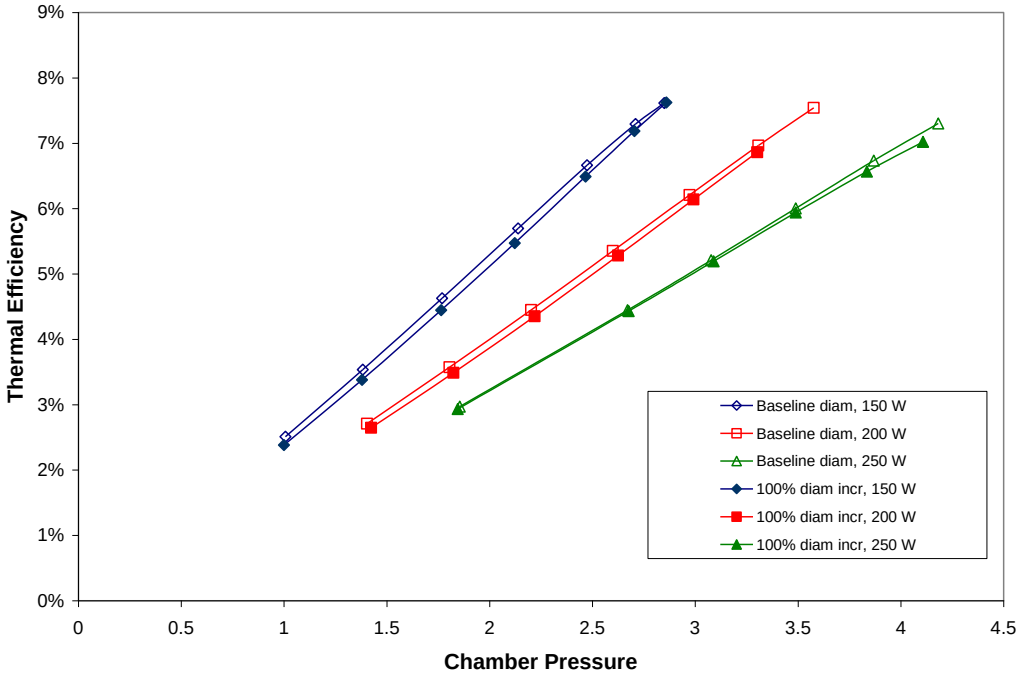

Figure 4.11 **Thermal efficiency vs. normalized chamber pressure comparison of injectors with a baseline diameter and a 100% increase of the baseline diameter at 150, 200, and 250 W using ammonia propellant.**

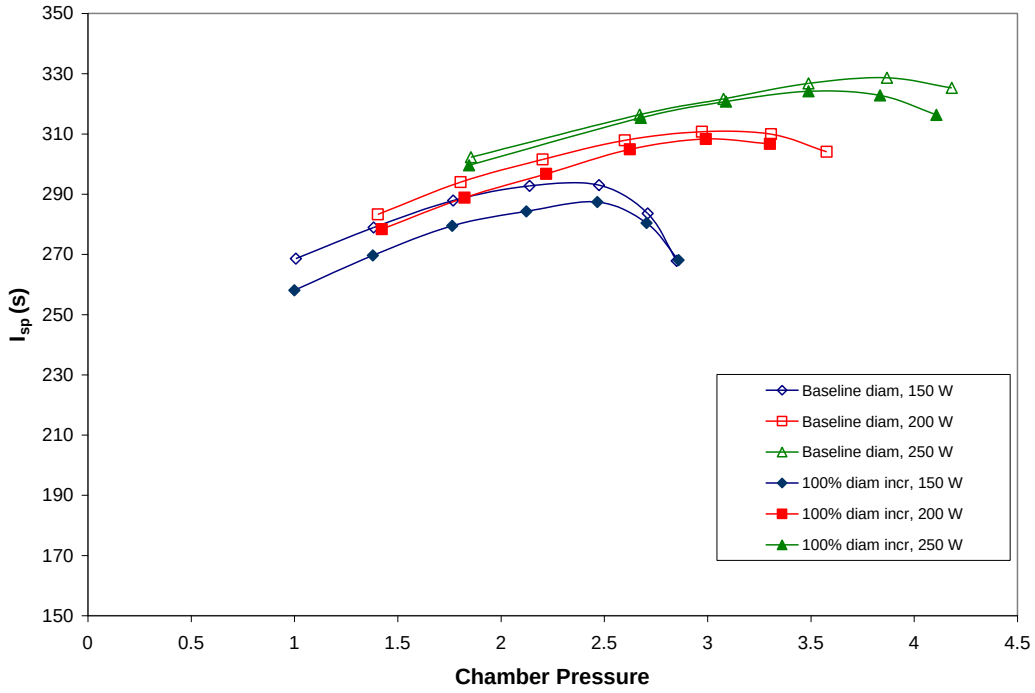

Figure 4.12 **Specific impulse vs. normalized chamber pressure comparison of injectors with a baseline diameter and a 100% increase of the baseline diameter at 150, 200, and 250 W using ammonia propellant.**

The data show that the maximum coupling efficiency is not greatly affected by injector diameter. In fact, the maximum coupling efficiency increases at 150 W for a larger injector diameter, remains constant at 200 W, and decreases at 250 W for a larger injector diameter. The thermal efficiency essentially remains unchanged when the injector diameter is increased for all power levels. The only relatively noticeable performance change is the specific impulse, which decreases as injector diameter is increased. However, a maximum exit velocity of the injector is reached when the injector is choked. At a constant upstream stagnation pressure (bottle pressure), the choked flow rate decreases for smaller injector diameters and, therefore, places a smaller limit on the maximum flow rate allowed through the injector. Increased mass flow in future tests prohibits the use of injectors with small diameters and therefore low choked flow rates because back pressures cannot be increased above the maximum pressure specifications of the flow controllers. Therefore the optimal injector diameter is the smallest diameter that does not choke the flow at a given bottle pressure.

4.3.1b Nozzle Optimization

The second flow control component of the MET is the nozzle. The nozzle regulates the flow exiting the chamber. The nozzle is parameterized by the diameter of the nozzle throat and the material from which it is constructed. The nozzles used for performance optimization of the MET are all made from stainless steel, save for one made from tungsten. The throat diameters of the nozzles incrementally increase from small to large, beginning with a baseline diameter and increasing by 20%, 72%, 150%, 200%, and 235%. The values calculated for performance evaluation and ultimate optimization include the same values used for the injector optimization, these being coupling efficiency, thermal efficiency, and specific impulse. Thruster efficiency, defined in Chapter 1, is also calculated in order to provide the overall efficiency of the MET. These four values are plotted against both normalized chamber pressure and normalized specific power. The results shown in Figures 4.13 through 4.20 depict a series of tests in which each test consists of a constant nozzle throat diameter that is exposed to at least three fixed forward power levels (150, 200, and 250 W). Two additional high power tests (300 and 350 W) were performed on the highest performing nozzles in order to observe increases in the performance of the nozzle.

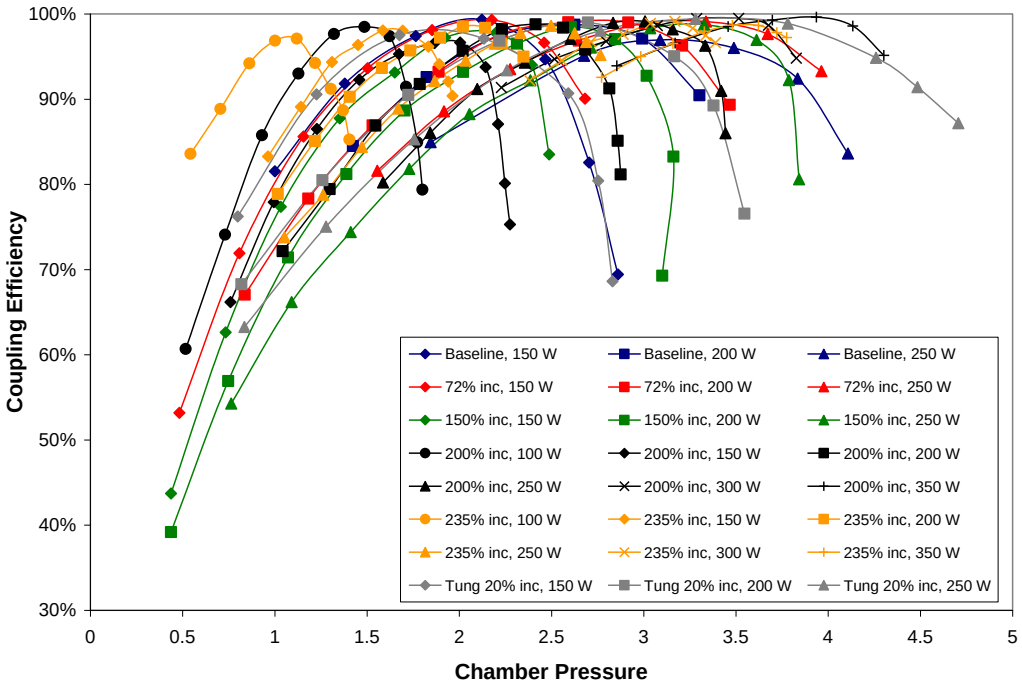

Figure 4.13 **Coupling efficiency vs. normalized chamber pressure for various nozzles using ammonia propellant.**

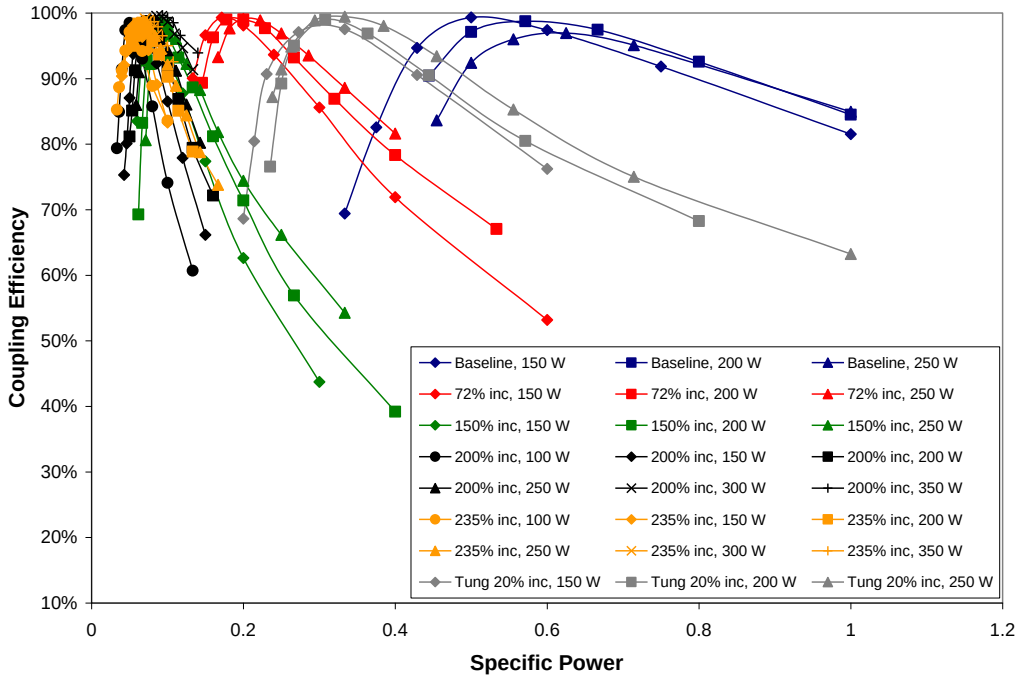

Figure 4.14 **Coupling efficiency vs. normalized specific power for various nozzles using ammonia propellant.**

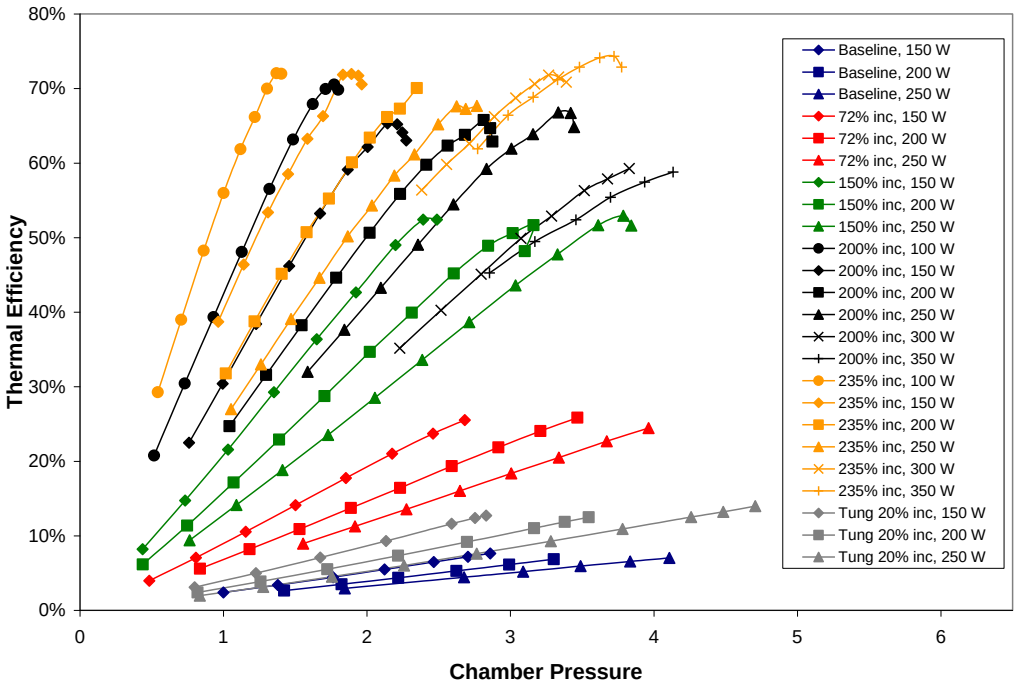

Figure 4.15 **Thermal efficiency vs. normalized chamber pressure for various nozzles using ammonia propellant.**

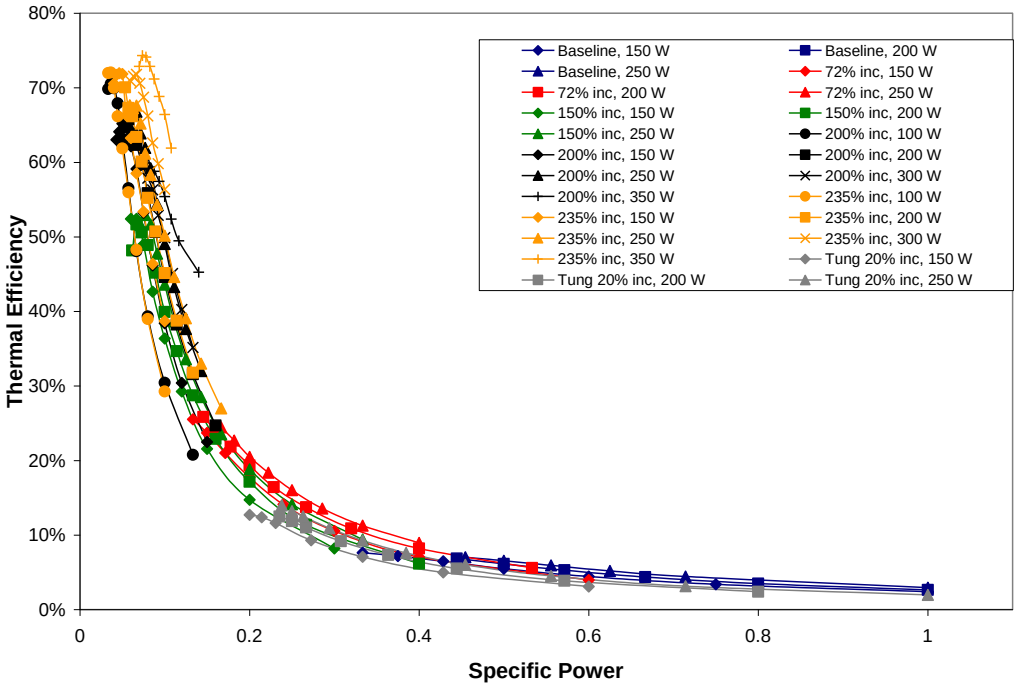

Figure 4.16 **Thermal efficiency vs. normalized specific power for various nozzles using ammonia propellant.**

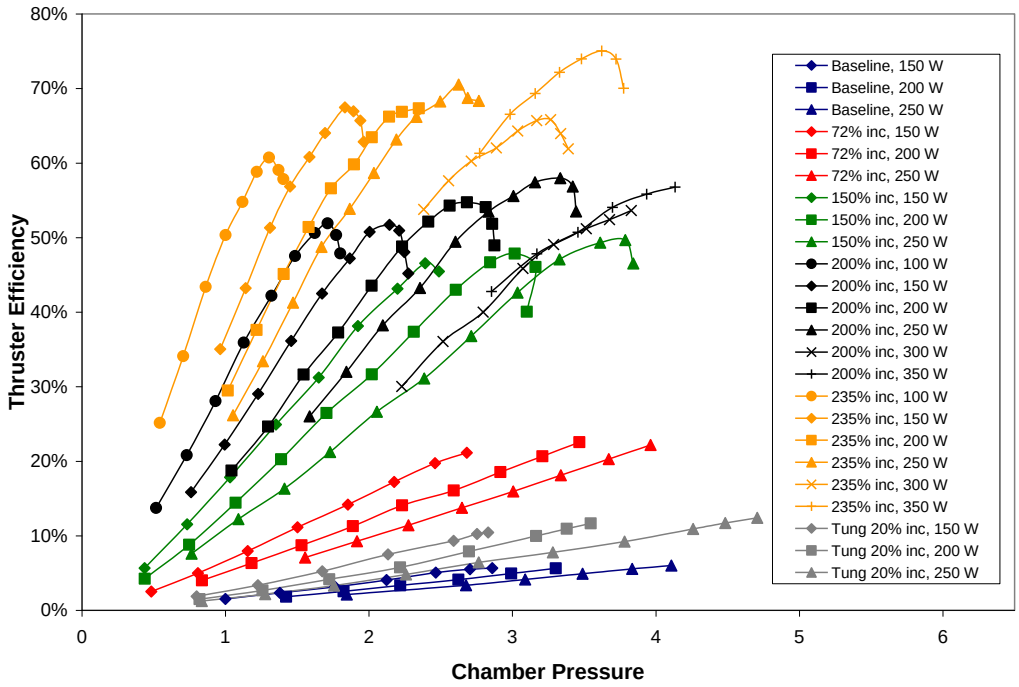

Figure 4.17 **Thruster efficiency vs. normalized chamber pressure for various nozzles using ammonia propellant.**

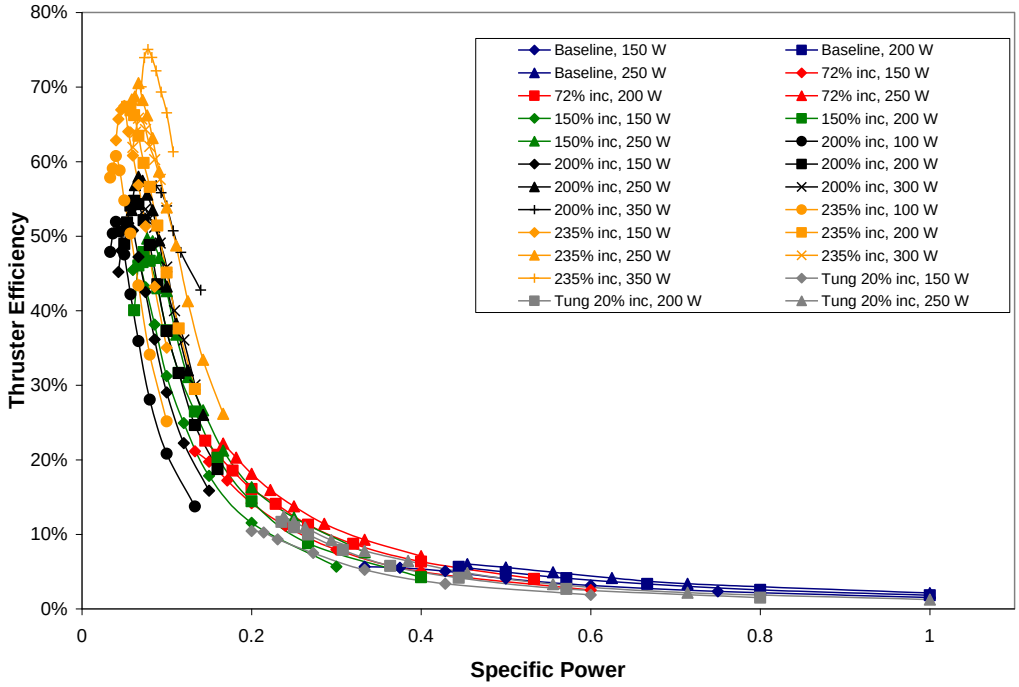

Figure 4.18 **Thruster efficiency vs. normalized specific power for various nozzles using ammonia propellant.**

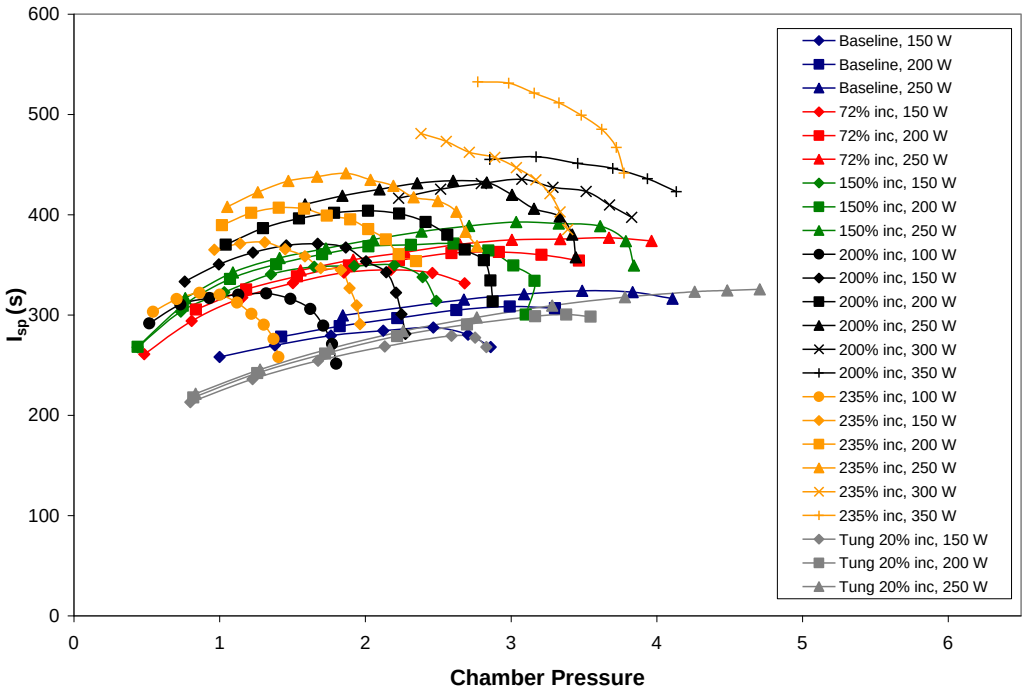

Figure 4.19 **Specific Impulse vs. normalized chamber pressure for various nozzles using ammonia propellant.**

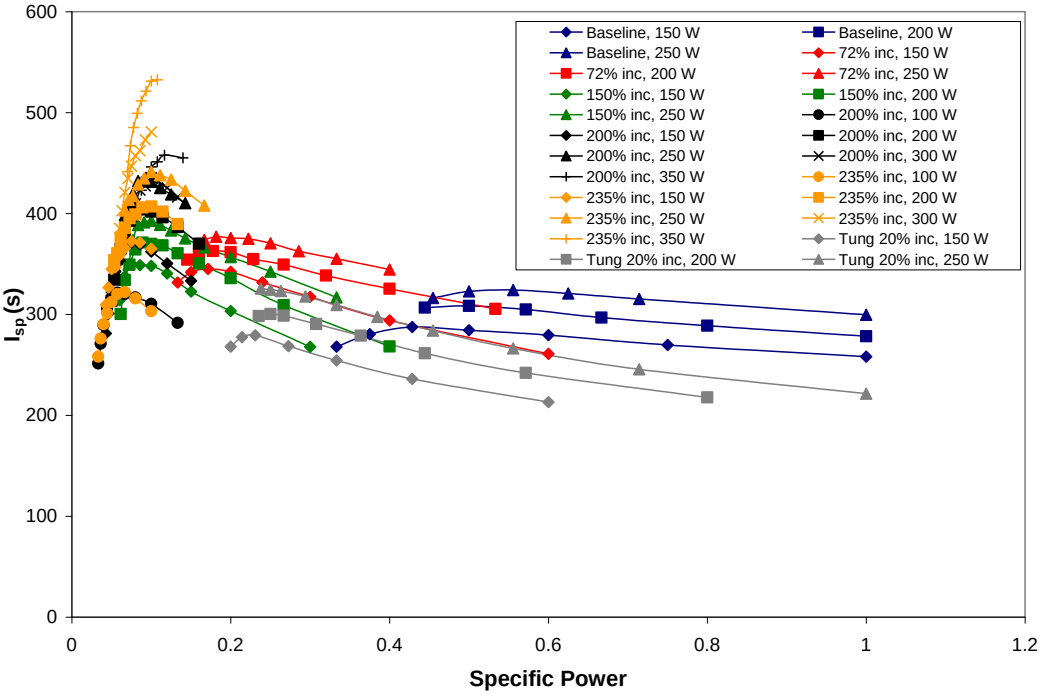

Figure 4.20 **Specific impulse vs. normalized specific power for various nozzles using ammonia propellant.**

All of the nozzles attain approximately the same maximum coupling efficiency, regardless of the input power, specific power, or chamber pressure. However, as the input power is increased, the maximum coupling efficiency occurs at higher chamber pressures for all nozzle configurations. This finding implies that an increase in power requires an increase in chamber pressure and, therefore, flow rate to maintain the maximum coupling efficiency of the thruster configuration.

The thermal efficiency increases with chamber pressure and, in turn, increasing mass flow. This is not only evident within each test, but throughout the entire nozzle comparison. Larger nozzles that require higher flow rates have significantly better thermal efficiencies than smaller nozzles with lower flow rates. This finding is reinforced by the fact that lower specific powers result in higher thermal efficiencies. The observation that the input power level does not have a large effect on the thermal efficiency of the configuration implies that thermal efficiencies are dependent mostly on specific powers, instead of absolute power. One interesting note about the thermal efficiency data is that the maximum thermal efficiency does not correspond to the maximum coupling efficiency, but instead occurs at higher chamber pressures. This is more proof that an increase in thermal efficiency is directly related to an increase in specific power, no matter the amount of absorbed power. Another interesting note about the thermal efficiency data is that the configuration using the tungsten nozzle does not produce thermal efficiencies as high as a stainless steel nozzle of similar throat diameter. This can be attributed to the fact that tungsten has a larger thermal conductivity value than steel and, in turn, conducts more heat out of the system. The optimized nozzle configuration with regard to thermal efficiency seems to have reached its maximum based on similar results from the two largest nozzles.

Conclusions reached from the thermal efficiency data are echoed by the thruster efficiency data. That is, that specific power is the driving force behind thruster efficiency. However, it should be noted that, although the optimal nozzle configuration seems to have been reached in the case of thermal efficiency, this is not the case with regard to thruster efficiency. The largest nozzle, 235% throat diameter increase from baseline, has significantly higher thruster efficiencies than the second largest nozzle,

200% throat diameter increase from baseline. The data shows that higher thruster efficiencies can still possibly be attained using nozzles with larger throat diameters.

The data show that specific impulse increases with input power. This is expected based on the definition of specific impulse; increasing exhaust velocity results in higher specific impulse, which occurs when the input power increases. The specific impulse also increases with increasing chamber pressure and decreasing specific power (i.e., mass flow); however, this trend only occurs up to a certain chamber pressure and specific power. It is interesting to observe that this highest performing pressure location occurs at different points depending on the nozzle configuration and, therefore, flow rate. However, the specific power values corresponding to these pressures are all relatively equal. This finding implies that there exists a minimum specific power value at which specific impulse is optimized. The largest nozzle configuration tested, the 235% throat diameter increase from baseline, seems to have reached that optimal minimum specific power. However, increasing input power still significantly improves specific impulse, no matter the specific power value. It should be noted that the tungsten nozzle has the lowest specific impulse observed. Again, this can be attributed to the fact that its thermal conductivity is higher than that of stainless steel.

The optimal nozzle configuration tested with regard to all four performance values is the largest nozzle, the 235% throat diameter increase from baseline. However, higher input power will most assuredly increase the specific impulse and, possibly, the thruster efficiency, which does not appear to have reached a maximum. The maximum specific impulse reached by this optimal nozzle, injector, and antenna depth configuration exceeds the specific impulse predicted by Clemens[18] for simulated hydrazine at 350 W by approximately 40%.

4.4 Simulated 50% Decomposed Hydrazine Results

Hydrazine is used in various operational propellant systems, which makes it a readily available propellant. The configuration of the MET used for simulated 50% decomposed hydrazine tests use the optimal antenna depth and injector size determined from the ammonia testing. The nozzle throat diameter was the only component

parameterized for optimization testing. The three nozzles used for this set of testing are the two largest nozzles used in ammonia testing and an additional nozzle that has a throat diameter 268% larger than the baseline nozzle used for ammonia testing. Coupling efficiency, thermal efficiency, thruster efficiency, and specific impulse are once again plotted against chamber pressure and specific power in order to asses the performance of the MET. Figures 4.21 through 4.28 display the results of the simulated 50% decomposed hydrazine optimization testing. Again, the chamber pressure and specific power are normalized to the same testing configuration used to normalize the ammonia data.

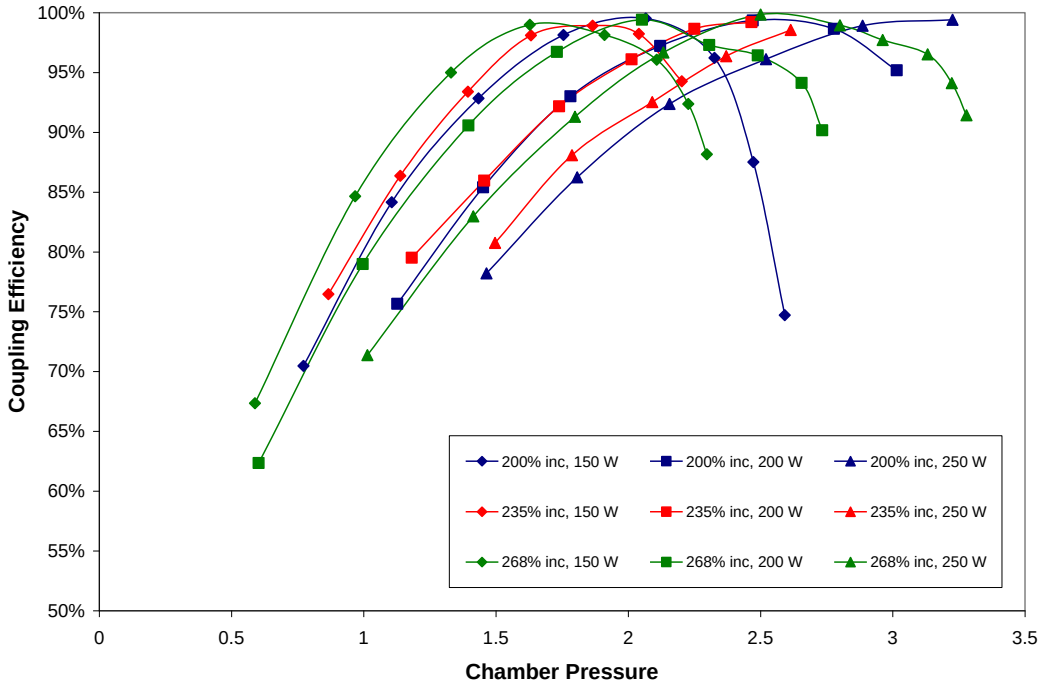

Figure 4.21 **Coupling efficiency vs. normalized chamber pressure for various nozzles using 50% cold decomposed hydrazine propellant.**

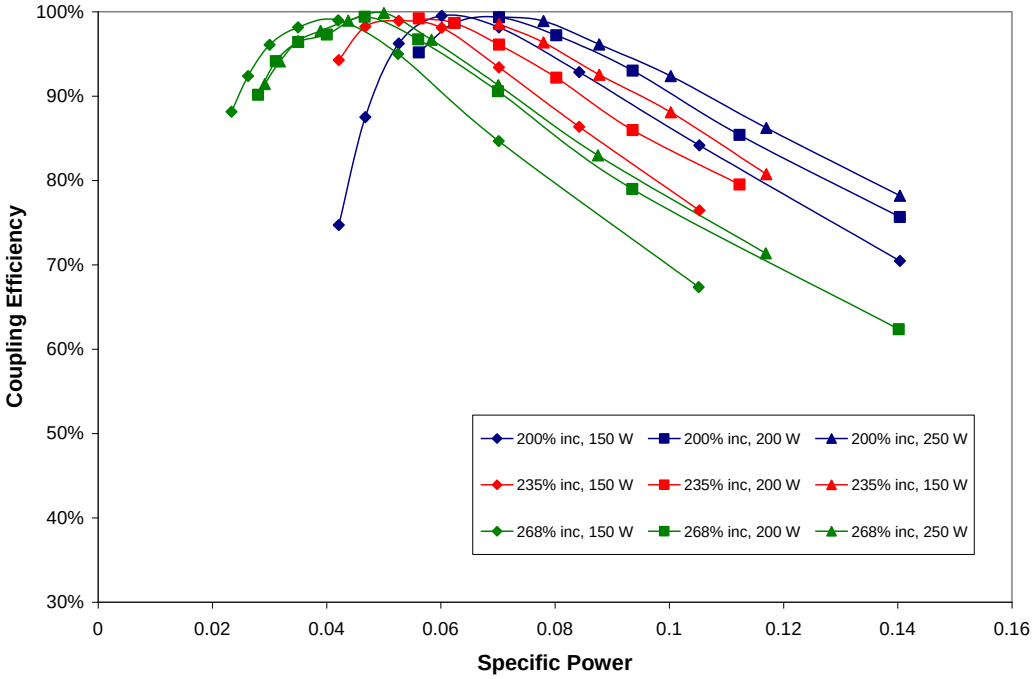

Figure 4.22 **Coupling efficiency vs. normalized specific power for various nozzles using 50% cold decomposed hydrazine propellant.**

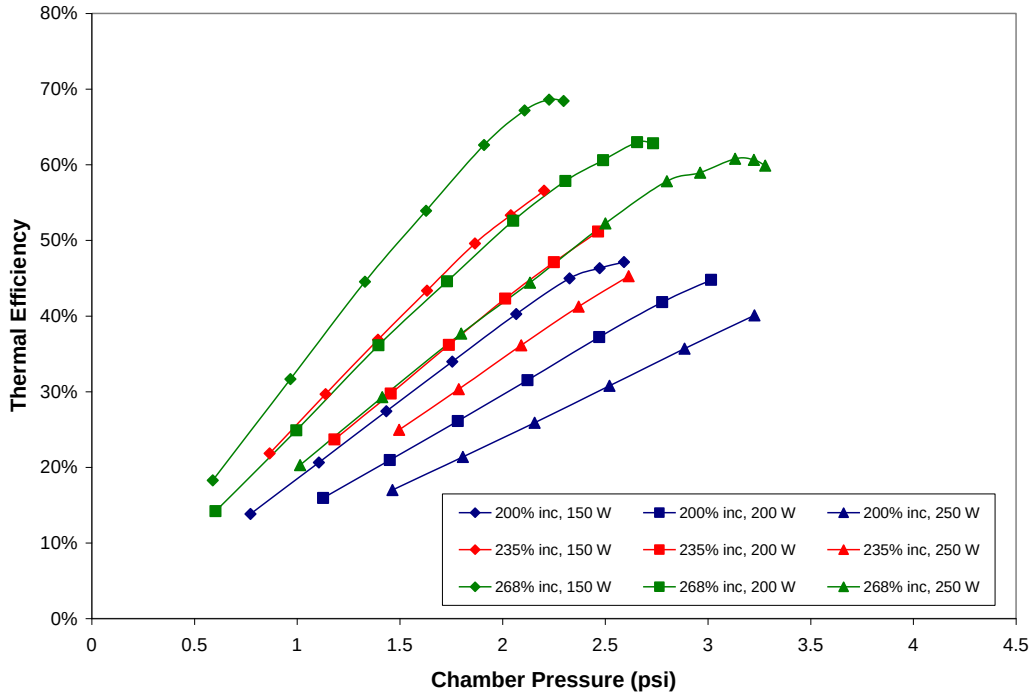

Figure 4.23 **Thermal efficiency vs. normalized chamber pressure for various nozzles using 50% cold decomposed hydrazine propellant.**

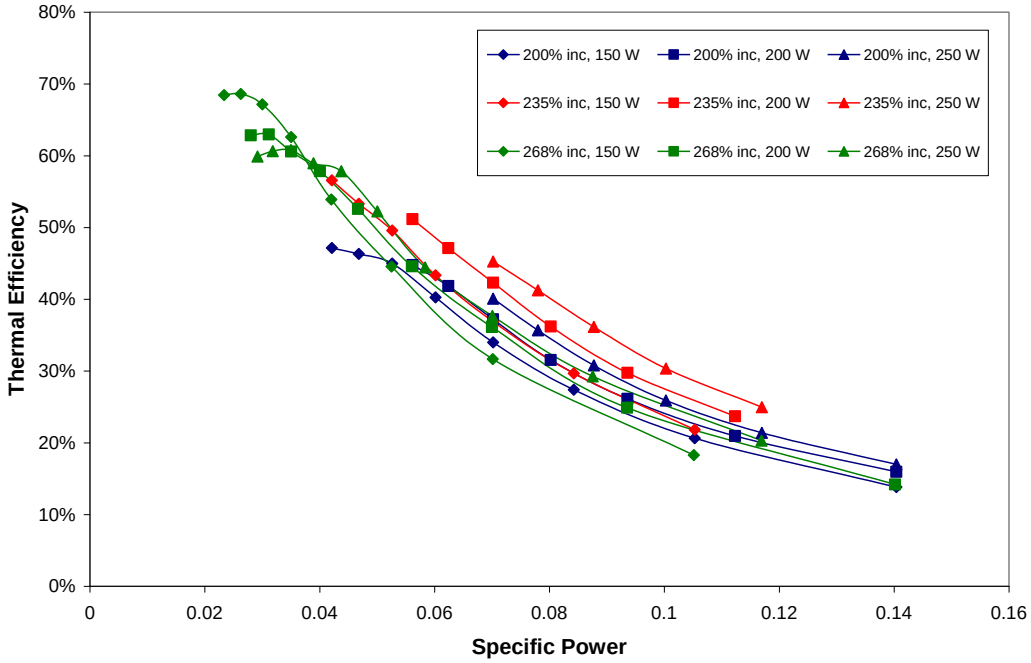

Figure 4.24 **Thermal efficiency vs. normalized specific power for various nozzles using 50% cold decomposed hydrazine propellant.**

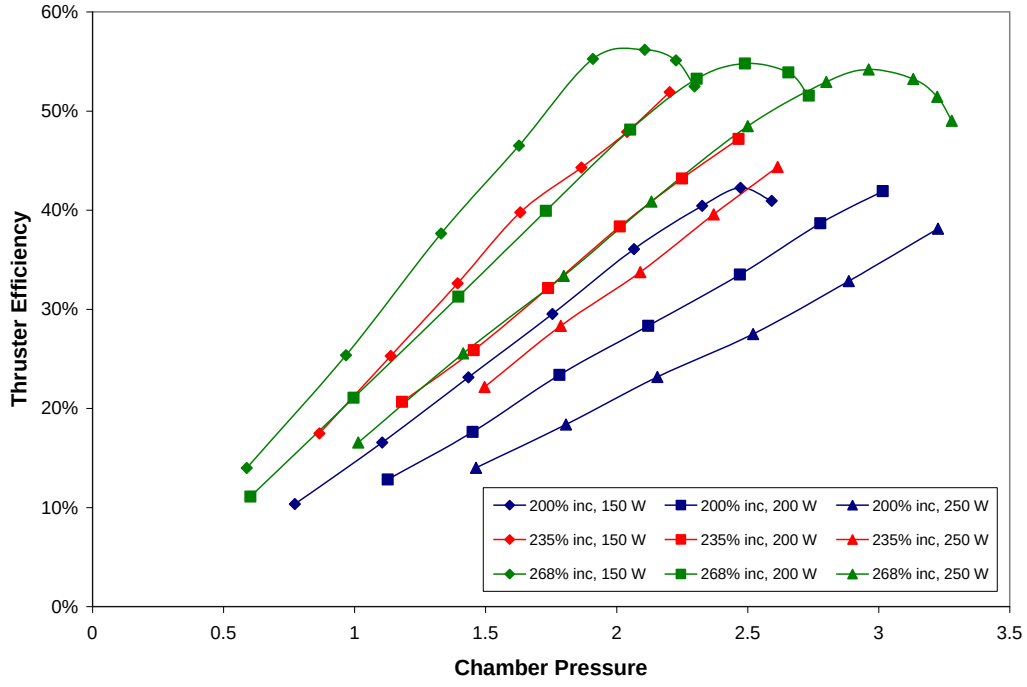

Figure 4.25 **Thruster efficiency vs. normalized chamber pressure for various nozzles using 50% cold decomposed hydrazine propellant.**

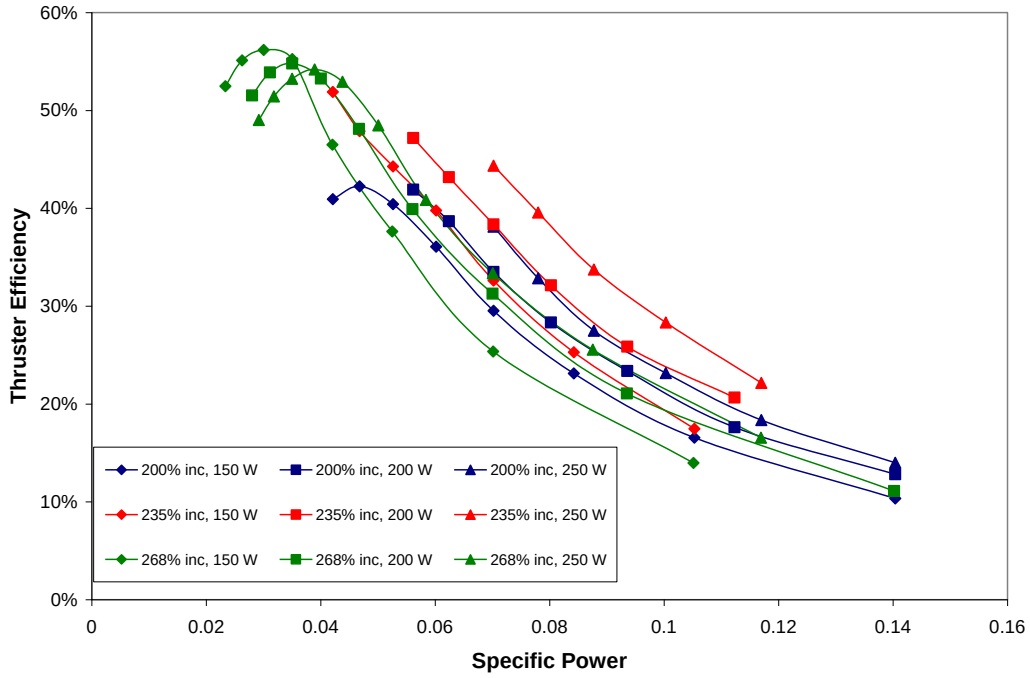

Figure 4.26 **Thruster efficiency vs. normalized specific power for various nozzles using 50% cold decomposed hydrazine propellant.**

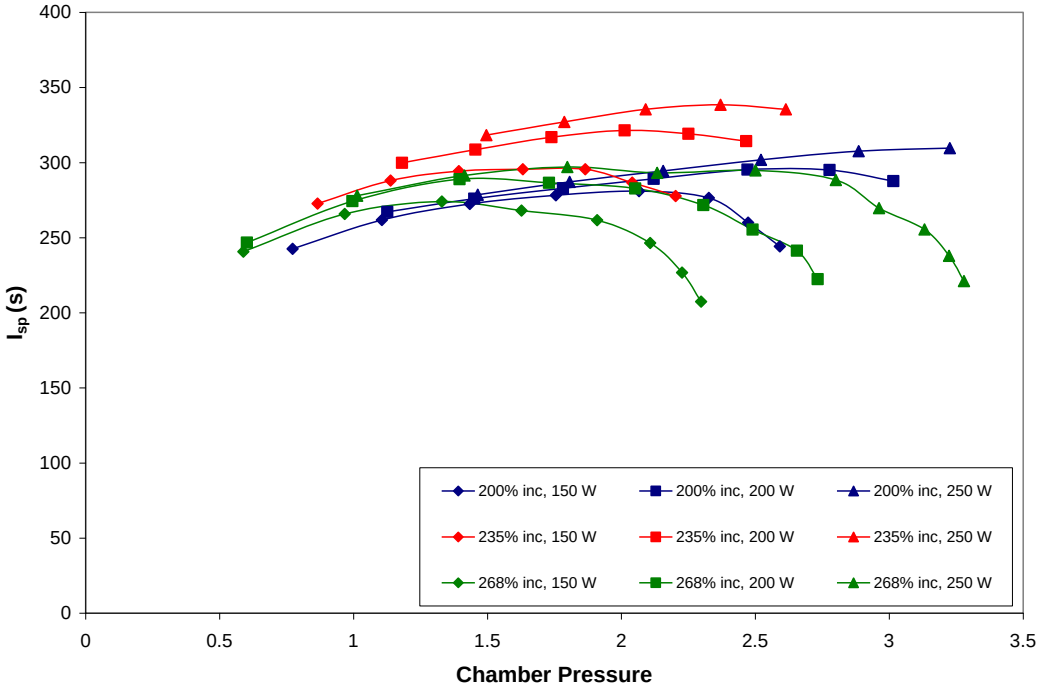

Figure 4.27 **Specific impulse vs. normalized chamber pressure for various nozzles using 50% cold decomposed hydrazine propellant.**

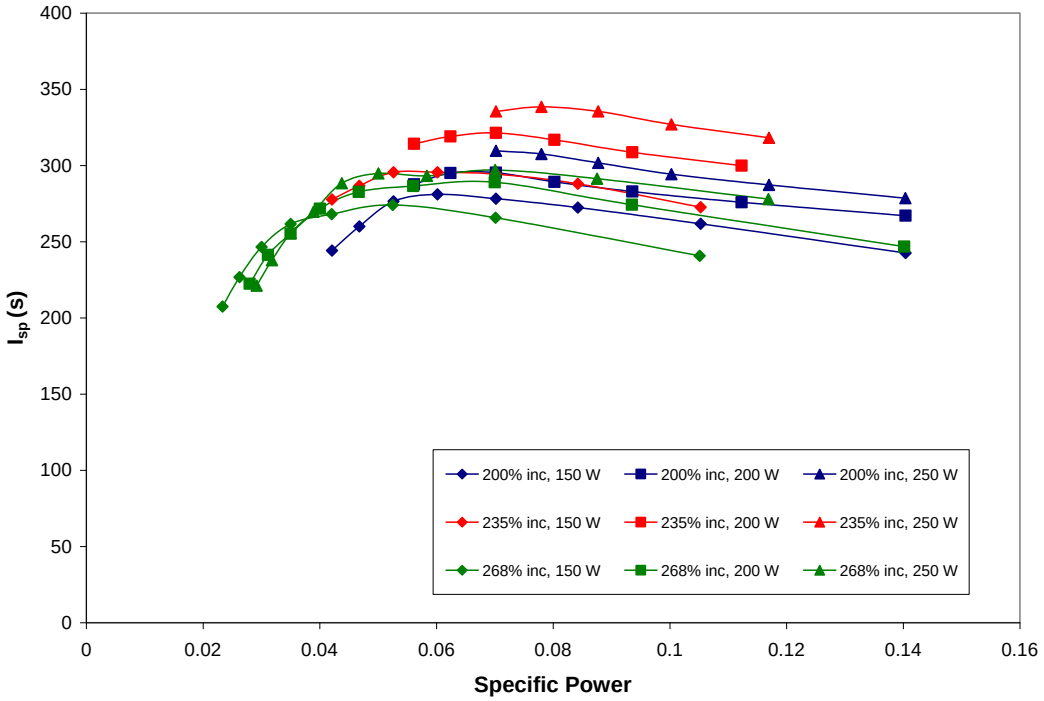

Figure 4.28 **Specific impulse vs. normalized specific power for various nozzles using 50% cold decomposed hydrazine propellant.**

The coupling efficiencies present in these results behave in the same manner as the ammonia data. In order to maintain maximum coupling efficiency when increasing power, an increase in mass flow is required. Thermal and thruster efficiencies of the simulated hydrazine also behave similarly to ammonia. A decrease in specific power results in an increase in these efficiencies. However, maximum thermal and thruster efficiencies do not appear to be attained. Nozzles with larger throat diameters need to be tested to verify these observations.

The specific impulse data are not as similar to the ammonia specific impulse results are as the other performance evaluation values. Similar to the ammonia data, a minimum specific power value seems to exist. However, unlike ammonia, the maximum specific impulse is not attained with the nozzle configuration that achieves the lowest specific power. Instead the configuration using a nozzle with a throat area 235% larger than the baseline throat diameter is the highest performing nozzle. Once again as expected, specific impulse increases as input power increases.

It should be noted that the maximum thermal efficiency, maximum thruster efficiency, and maximum specific impulse observed for the simulated hydrazine tests are all less than the maxima observed from the ammonia tests, indicating that either the absolute simulated hydrazine maxima have yet to be attained or ammonia is a superior propellant. However, the maximum simulated 50% decomposed hydrazine specific impulse observed through this set of testing exceeds Clemens[18] experimental maximum simulated 100% decomposed hydrazine specific impulse value by approximately 10%.

CHAPTER 5
Conclusions and Recommendations

The objective of the 8-GHz MET research presented in this thesis was to both obtain direct thrust measurements using a well calibrated, functioning thrust stand, and optimize the thruster configuration in order to achieve the best possible performance. Presented below is an analysis of the findings of these series of tests and recommendations for future research.

The ability to accurately measure thrust using a fixed thrust stand was not reached. However, information about the mechanisms acting on the thrust stand was gathered and can be used for further thrust measurement research. The momentum trap showed an inability to measure small thrust values, but this problem was corrected when the deflection cone was implemented. Thermal drift caused the strain gauge to report inflated thrust measurements, but this problem was corrected when the optical sensor was used instead. There are unknown loss mechanisms causing the measured thrust to be less than the theoretical thrust. Further study of these loss mechanisms will lead to the correction of this problem. Thrust values can also be attained through various direct thrust methods in which the thruster is either counterbalanced or fixed directly on a load cell.

The nitrogen testing showed that a one-piece thruster design cannot function over an extended period of time. Plasma created at the base of the thruster ultimately destroys the antenna and results in the inability of the MET to function. Antenna caps constructed from a material with a higher heat resistance could provide the needed protection for the antenna. Otherwise, it seems that a separation plate is required to operate the MET. The nitrogen testing also showed that a separation plate does not impede the performance of the thruster.

An optimized thruster configuration was determined when using ammonia propellant. The antenna depth is to be set at a 75% reduction of the baseline depth. The injector diameter size is to be the smallest possible without choking the flow. The nozzle throat diameter is to be 235% larger than the baseline throat diameter. This configuration

produced the highest specific impulse ever attained by any MET configuration using ammonia propellant, approximately 33% higher than the maximum specific impulse achieved by the 2.45-GHz MET.[18] Significantly high efficiencies were achieved as well. However, because maximum thruster efficiency does not appear to have been reached, nozzles with larger throat diameters should be considered for testing. Higher power (400 W to 1000 W or higher) tests should be performed to obtain greater thruster performance. Finally, a nozzle constructed from a material with a lower thermal conductivity value than stainless steel should improve performance and be considered for testing.

Although specific impulse values attained through the simulated 50% decomposed hydrazine tests are greater than those recorded by Clemens[18], simulated 50% decomposed hydrazine data showed that an optimal thruster configuration has yet to be determined. Nozzles with larger throat diameters may improve specific impulse and will likely improve thermal and thruster efficiencies. As with ammonia, a nozzle constructed from a lower thermal conductivity material as well as higher input power levels should also improve the performance of the thruster. Thruster optimization using simulated 80% decomposed hydrazine also must be conducted in order to determine the highest performing composition of simulated decomposed hydrazine products.

REFERENCES

1) Hill, P. and Peterson, C., *Mechanics and Thermodynamics of Propulsion*, 2nd Edition, Addison-Wesley Publishing Company, Inc., New York, 1992.

2) Larson, W. and Wertz, J., *Space Mission Analysis and Design*, 3rd Edition, Microcosm Press and Kluwer Academic Publishers, Boston, 1999.

3) Anderson, J., *Modern Compressible Flow*, International Edition, The McGraw-Hill Companies, Inc., New York, 2004.

4) Balaam, P., Maul, W., and Micci, M. M., "Characteristics of free floating nitrogen and helium plasmas generated in a microwave resonant cavity," IEPC-88-099, 20th DGLR AIAA JSASS International Electric Propulsion Conference, Garmisch Partenkirchen, W. Germany, Oct 1988.

5) Balaam, P. and Micci, M. "Investigation of free floating nitrogen and helium plasmas generated in a microwave resonant cavity," AIAA-89-2380, 25th AIAA/ASME/SAE/ASEE Joint Propulsion Conference, Monterey, CA, July 1989.

6) Sullivan, D. J. and Micci, M., "The Effect of molecular propellants on the performance of resonant cavity electrothermal thrusters," IEPC-91-034, 22nd DGLR AIAA JSASS International Electric Propulsion Conference, Viareggio, Italy, Oct 1991.

7) Mueller, J., *Performance Evaluation and Operating Characteristics of a Waveguide Microwave Applicator for Space Propulsion Applications*, Ph.D. Dissertation, Department of Aerospace Engineering, The Pennsylvania State University, 1993.

8) Sullivan, D., *Development and Performance Characterization of a Microwave Electrothermal Thruster Prototype*, Ph.D. Dissertation, Department of Aerospace Engineering, The Pennsylvania State University, 1995.

9) Kline, J., *Thrust Measurements of a Microwave Electrothermal Thruster*, Master of Science Thesis, Department of Aerospace Engineering, The Pennsylvania State University, 1996.

10) Nordling, D., *High-Frequency Low-Power Microwave Arcjet Thruster Development*, Master of Science Thesis, Department of Aerospace Engineering, The Pennsylvania State University, 1998.

11) Souliez, F., *Low-Power Microwave Arcjet Spectroscopic Diagnostics and Performance Evaluation*, Master of Science Thesis, Department of Aerospace Engineering, The Pennsylvania State University, 1999.

12) Roos, C., *Vertical-Deflection Thrust Stand Measurements of a Low Power Microwave Arcjet Thruster*, Master of Science Thesis, Department of Aerospace Engineering, The Pennsylvania State University, 2001.

13) Souliez, F., Chianese, S., Dizac, G., and Micci, M., "Low Power microwave arcjet testing: Plasma and plume diagnostics and performance evaluation," AIAA-99-2717, 35th AIAA/ASME/SAE/ASEE Joint Propulsion Conference, Los Angeles, CA, June 1999.

14) Welander, B., *Low-Power Microwave Arcjet Thruster Using Nitrogen Propellant*, Master of Science Thesis, Department of Aerospace Engineering, The Pennsylvania State University, 2004.

15) Diamant, K., Cohen, R., and Brandenburg, J., "High Power microwave electrothermal thruster performance on water," AIAA-2002-3622, 38th AIAA/ASME/SAE/ASEE Joint Propulsion Conference, Indianapolis, IN, July 2002.

16) Clemens, D., *Performance Evaluation of a Low-Power Microwave Electrothermal Thruster*, Master of Science Thesis, Department of Aerospace Engineering, The Pennsylvania State University, 2004.

17) Goovaerts, K., *Feasibility Studies of a 14.5 GHz, Low Power Microwave Electrothermal Thruster*, Master of Science Thesis, Department of Aerospace Engineering, The Pennsylvania State University, 2007.

18) Clemens, D., *Performance Evaluation of the Microwave Electrothermal Thruster Using Nitrogen, Simulated Hydrazine, and Ammonia*, Ph.D. Dissertation, Department of Aerospace Engineering, The Pennsylvania State University, 2008.

19) Pozar, D.M., *Microwave Engineering*, John Wiley & Sons, Inc., 3rd Edition, Hoboken, 2005.

20) Balanis, C. A., *Advanced Engineering Electromagnetics*, John Wiley & Sons, Inc., Hoboken, 1989

21) Chen, F. F., *Introduction to Plasma Physics and Controlled Fusion*, 2nd Edition, Springer Science + Business Media, LLC, New York, 2006.

22) Raizer, Y. P., *Gas Discharge Physics*, Springer-Verlag, Berlin, 1991.

23) Borman, G. and Ragland, K., *Combustion Engineering*, WBC/McGraw Hill, New York, 1998.

24) Schmidt, E. W., *Hydrazine and Its Derivatives: Preparation, Properties, Applications*, John Wiley & Sons, Inc., New York, 2001.